12-2012

IMPEDANCE-BASED FAULT LOCATION METHODS FOR TRANSMISSION LINE CONNECTING WIND FARM PLANTS

Chaoqi Ji
Clemson University, cji@g.clemson.edu

IMPEDANCE-BASED FAULT LOCATION METHODS FOR TRANSMISSION LINE CONNECTING WIND FARM PLANTS

A Thesis
Presented to
the Graduate School of
Clemson University

In Partial Fulfillment
of the Requirements for the Degree
Master of Science
Electrical Engineering

---

by
Chaoqi Ji
December 2012

Accepted by:
Dr. Elham B. Makram, Committee Chair
Dr. Richard Groff
Dr. John Gowdy

ABSTRACT

With an increasing capacity of wind power installed in the world, the impact of wind generation during fault condition has been studied. Wind plants equipped with induction generator results in a different fault behavior in transmission networks. In this paper, the validation of existing impedance-based fault location methods are performed on a transmission line connecting wind plant equipped with three different types of induction generators. This work is based on the simulation in real-time digital simulator (RTDS).

Squirrel-cage induction generator (SCIG), wound-rotor induction generator (WRIG) and doubly-fed induction generator (DFIG) are the three common generators used for wind power plants. Therefore, models for these induction generators are developed and the control schemes for each type are simulated to represent a working wind plant. Pitch angle control and variable slip control are applied to SCIG and WRIG respectively to maintain a constant power output of the wind generators. DFIG utilizes vector control strategy to control the power output of the wind generators independently.

After the wind plant model is developed, it is connected to an equivalent transmission line system. A fault is simulated on the transmission line so that the fault location algorithm can be applied to determine the fault location estimation with the existence of wind plant.

Results of fault location estimation are compared and discussed when fault location algorithms are applied to transmission line system connecting different induction

generator-based wind plant. It is validated that certain fault location algorithms are not accurate for transmission line connecting wind plant.

DEDICATION

This thesis is dedicated to my parents and all my friends I met during my graduate study at Clemson University. Thank you all for your help and support.

ACKNOWLEDGMENTS

I would like to extend my sincere thanks to my advisor, Dr. Elham B. Makram, for her assistance, guidance and encouragement throughout my research. I would also like to thank Dr. Richard Groff and Dr. John Gowdy for providing many hours of discussion and for serving on my committee.

TABLE OF CONTENTS

Page

Table of Contents (Continued) Page

LIST OF TABLES

List of Tables (Continued)

Table Page

LIST OF FIGURES

List of Figures (Continued)

Figure Page

List of Figures (Continued)

Figure Page

List of Figures (Continued)

Figure Page

CHAPTER ONE

INTRODUCTION AND LITERATURE REVIEW

1.1 Overview of Fault Location Techniques

The modern electric power system is a large and complex network that consists of thousands of transmission and distribution lines. With a growing demand of electricity, this number is increasing. Transmission and distribution lines experience faults that are caused by severe weather, animals and equipment malfunction, etc. Most of the faults are temporary and can be removed by devices like automatic recloser. Temporary faults do not affect power supply permanently and generally require no human operations. Others are permanent faults when maintenance crews are sent to the fault location to repair the damage and restore the power supply. Since customers in today's society are more sensitive to power outages, the modern power system is required to be safer and more reliable. Therefore, an estimation of fault location with reasonable accuracy can greatly help the engineers identify the fault equipment and speed up the recovery of power supply.

Nowadays, many protective relays installed on the transmission and distribution lines are able to automatically estimate the fault location of the protected line by processing certain signals. Based on the signal used, fault location techniques are classified into three different categories [1]:

1. Techniques based on fundamental-frequency of voltages and currents
2. Techniques based on high-frequency travelling waves generated by faults
3. Artificial intelligence approaches

Fault location techniques using fundamental-frequency components, also known as impedance-based fault location methods, extract the fundamental-frequency components of the voltage and current signals to calculate the impedance of the faulted line. The calculated impedance is considered to be a measure of the distance to fault. An IEEE guide [2] listed some notable definitions for fault location estimation in modern electric power system. Fault location error is defined as the percentage error in fault location estimate based on the total line length. Homogeneous line is a transmission line where impedance is distributed uniformly on the whole length. These two definitions will be used many times in the application of impedance-based fault location techniques.

Impedance-based method is widely used in modern protective relays because of easy implementation. It can be further classified into one-end or two-end depending on how many terminal voltages and currents are required [3].

One-end impedance-based method uses the voltage and current captured at one terminal of the line. It is a straightforward algorithm and requires simple communication channels. Positive-sequence-reactance method calculated the apparent impedance seen by one terminal based on the voltage and current measurements [2]. Fault resistance was assumed to be zero to simplify the fault location estimation. Therefore, this method introduces an increasing error as the fault resistance increases.

Takagi [4] calculated the reactance of a faulted line by using voltage and current data at one end of the transmission line. The effect of load flow was eliminated by subtracting pre-fault load current from the captured fault current. The effect of fault

resistance was also removed by assuming that the phase angles of the total fault current and the fault current from the measured terminal are equal.

Izykowski [5] utilized complete voltage and current measurements at one end to locate a fault on a parallel transmission line. The effectiveness and accuracy of the method was proved by an Electromagnetic Transients Program (EMTP) simulation.

Girgis [6] was able to use the recursively updated voltage and current vector data at a single location to estimate the distance of the fault in a radial distribution system by apparent impedance approach using symmetrical components of the line impedance. The voltage and current vectors at the one end were obtained by a load flow program and updated after each recursion. Based on the line construction configuration, the line impedance matrix was obtained to calculate the voltage drop for each line section in the downstream. The load current injected at each line section end was calculated based on the assumption of static impedance load model. Some features of power distribution systems such as multiphase laterals, unbalanced conditions and unsymmetrical nature were taken into account by using this method. Test case showed accurate fault location obtained from an EMTP simulation.

A fault location method for distribution feeders using fault circuit indicators (FCIs) and intelligent electronic devices (IEDs) was presented by Gong [7]. Considering the complex topology of the distribution system, this impedance-based method utilized all the devices that can record and transfer voltage and current data to help identify the fault location. Fault location algorithm was performed at the IED that is closest to the fault and

FCIs were used to narrow the possible fault locations. Field tests were made to compare the results of traditional methods and the estimations were proved to be more accurate.

Choi [8] developed a fault location algorithm using direct three-phase circuit analysis for unbalanced distribution system. This method considers the unbalanced distribution laterals and loads. Instead of using symmetrical components, the three-phase impedance matrix obtained by Carson's line theory [9] was calculated considering the unbalanced characteristics of the distribution line. A simulation using EMTP was performed in this paper. The fault distance calculated from the algorithm was compared with the actual fault distance with reasonable accuracy.

Two-end fault location method processes data from both terminals of the line. Therefore, it requires more investments on effective communication channels. Compared with one-end method, two-end method provides fault location estimation more accurately. A fault location approach for multi-terminal transmission lines was proposed by Tziouvaras et. al. [10]. This method utilizes the magnitude of negative-sequence current and negative-sequence source impedance from all the remote terminals. Pre-fault load flow, zero-sequence mutual coupling, fault resistance, system non- homogeneity and current infeeds from other lines will not affect the accuracy of fault location estimation. Simulation in EMTP proved the validity of this method in two- and three-terminal transmission lines.

Girgis [11] developed a two-end fault location algorithm by using three-phase line impedance matrix instead of symmetrical components. The line configuration, three-phase voltage and current data at all terminals were required as input signals. The

advantage of this method is that it also applies to unbalanced distribution lines if voltage and current data at both terminals are available. Fault location algorithms with synchronized and unsynchronized data were derived in this paper and the results showed high accuracy.

All the methods discussed above take fundamental-frequency components as the input signals. Alternatives for this are the fault location methods based on high-frequency travelling waves which utilize the forward and backward travelling high-frequency voltage or current waveforms generated by faults. These travelling waves contain the information of fault location and have been studied a long time ago [1]. It has been proved that this technique is not affected by power fundamental-frequency phenomena such as current transformer saturation, fault type, fault resistance and source parameters of the system. Thus, it can provide very accurate fault estimation. Although the requirement of high sampling rate of the digital data has been stated as the major limitation of its application, modern development of Global Positioning System (GPS) synchronization and communication system has emerged to solve this problem. Gale [12] and Magnago [13] described the application of travelling waves in fault location estimation and simulated a single transmission line in EMTP to validate the effectiveness.

Ibe [14] used the telegraph equations as the line model and measured voltage and current samples at one terminal of the line to create instantaneous voltage and current profiles. Both two- and three-terminal systems were simulated in this paper. The results proved that this method provided accurate estimation and was not affected by noise.

Bo [15] applied travelling-wave techniques to distribution overhead lines and underground cables. The simulation system was a simple distribution line with equivalent sources at both ends. Voltage and current data were captured at both terminals as input to determine the fault position. Simulation in EMTP showed that the accuracy of fault location estimation improves with higher digital sampling rate for overhead line and underground cable.

Fault location methods using travelling waves require very high sampling rate to show the advantage of high estimation accuracy and their implementation is more expensive than the implementation of impedance-based methods. Moreover, the application of travelling-wave methods is very limited in distribution system because of the complex topology and inadequate recording devices throughout the distribution networks. With the development of computation and communication techniques, a new type of fault location algorithm has been made using artificial intelligence (AI) approaches.

The introduction of AI in fault location algorithms starts with the consideration that AI techniques may help to increase the accuracy of estimation by pattern recognition and decision making approaches [1]. Three major families of AI techniques found in modern power system applications are artificial neural networks (ANN), expert system techniques and fuzzy-logic systems.

Li [16] developed a fault location method based on Artificial Neural Network (ANN). A 400kV two-source system was simulated. The algorithm was trained using

fault information captured at two terminals of the line. The results gave an accurate prediction of fault location and fault resistance.

Few applications of expert system techniques have been developed to fault location method because there is no extensive knowledge base available [1]. But it does solve some off-line task such as fault diagnosis and post fault analysis.

Galijasevic [17] et. al. presented a new method for short-circuit fault location estimation. The measured bus voltage sag patterns were compared with the pattern obtained by applying faults at different buses with assumed fault resistances. On-line and off-line simulations were performed to evaluate the validity of this method. The results obtained had acceptable errors.

Although the development of computation techniques has greatly promoted the application of AI in many fields, its application in electric power system remains limited due to the lack of mathematical theory and doubtable ability of correct decision for a huge system like power networks.

Some mature technologies are introduced to electric power system. Synchronized phasor measurement has been found to be the most powerful tool applied to power system in recent years in many aspects including system monitoring, protection, operation and control, etc [18].

Fan [19] developed an adaptive fault location technique based on phasor measurement unit (PMU) data for transmission lines. Voltage and current phasors from both terminals of the line were captured and calculated by online parameter-calculation algorithm. EMTP simulation with practical system data was performed to show that the

proposed method was able to locate fault accurately for different types of fault and various fault resistance.

A numerical algorithm for arc fault analysis was derived based on single line to ground fault on short overhead transmission lines [20]. The author built a dynamic arc model to represent the fault and applied a non-recursive parameter estimation method. The results from a simulation case provided accurate estimation of the arc voltage amplitude and fault location.

Korkali et al. [21] stated a fault location procedure based on travelling waves by wavelet transform. The arrival time of the travelling wave reflected from the fault point was extracted. The transient waveforms were all recorded upon synchronized sampling. Accurate estimation of the fault location was observed using very few PMU devices.

Mohammed [22] addressed a PMU-based fault location method for interconnected networks. An optimal placement of PMU devices was highlighted based on tree search method. The fault location algorithm was simulated on an 115kV system in PSCAD and MATLAB. The results gave estimations with acceptable errors.

In summary, different types of fault location techniques have been researched to provide accurate fault location estimation for different cases. Due to the complexity of the power networks, there are many factors that can affect the accuracy of fault location estimation [1]. They can be summarized as the following categories:

1. Inaccurate line model
2. Uniform line impedance assumption
3. Neglecting pre-fault load flow

4. Fault resistance including presence of an arc
5. Measurement errors

With the deregulation of the power industry, it is even desired to provide better service to the customers with sensitive loads. Also, with an increasing amount of renewable energy integrated to the existing power networks, engineers and researchers are facing new challenges to make electric power systems safer and more reliable.

1.2 Overview of Wind Power Integration

Wind power is the fastest growing source of renewable energy in the world. At the end of 2010, worldwide installed capacity of wind-powered generator was 197GW, with 40GW in US [23]. Each year, increasing portions of world electricity production is contributed by wind power. Denmark received 22% of its annual electric energy from wind generation; 17% of Portugal's load was served by wind, and the U.S. state of Texas produced 6.4% of its electricity from wind power [24].

Commercial bulk wind plants usually have dozens to hundreds of megawatt-class turbines ranging from 1 to more than 2 megawatt (MW) connecting a substantial medium-voltage network [25]. In North America, most commercial wind plants adopt induction generators rather than synchronous generators at the present time. Four types can be classified for commercial wind generators based on electrical topology. They are:

1. Standard squirrel-cage induction generator (SCIG) connected directly to the grid
2. Wound-rotor induction generator (WRIG) with variable rotor resistance
3. Doubly fed asynchronous generator

4. Synchronous or induction generator with full-size power converter

These plants exhibit different static and dynamic characteristics and do not fit the template for models of conventional generating facilities. Therefore, detailed models of wind generator and turbine will be the fundamental task for the analysis of wind integration. Fox et. al. [26] gave a brief introduction of the structure of different wind generators and their control strategies.

With the introduction of power electronics, many researchers have developed detailed models for Type 3 generator [27-29]. The most successful one connected a back-to-back converter across the stator and rotor side of the induction generator. This converter functions in two parts. One part is called the rotor-side converter (RSC), which controls the real and reactive power output from the stator winding. The other part is called grid-side converter (GSC), which maintains the DC voltage of the capacitor between the two converters. Specific control strategies are designed for this model to achieve independent control of real and reactive power. In this thesis, Chapter 3 will cover the details of the mathematical model and control design.

Short-circuit contribution to the transmission network from a wind plant equipped with Type 1 generator was estimated by Samaan [30]. The short-circuit analysis of power networks connecting wind turbines has been studied to demonstrate the impact of wind integration during fault conditions. Results showed that the wind plant contributed significant fault current during the initial cycle of an asymmetrical fault, but the contribution decayed as the fault persisted.

Morren [31] determined high short-circuit current contributed by wind turbine equipped with doubly-fed induction generator (DFIG). Less than 15% difference was observed between the results of approximate equations and time-domain simulation.

With an increasing capacity of wind plants installed and connected to existing electric power grids, there are concerns how wind integration will impact the grid and what changes are needed to introduce wind power safely. Reginato et. al [32] discussed the acceptable wind integration level based on three criteria: terminal voltage variation, power transfer margin and internal voltage angle. Two types of induction generator based wind turbines were modeled. One was squirrel cage induction generator with fixed speed and the other was doubly-fed induction generator with variable speed. Profiles of wind integration level limits were made for each criterion, as a function of the X/R ratio of the network impedance.

Engineers and researchers are dedicating their efforts to accurately model the wind plants so that practical results can be achieved to analyze the characteristics for better and safe use of this green energy.

1.3 Thesis Overview

The purpose of this thesis is to examine the application of conventional impedance-based fault location methods for transmission line connecting a wind power plant equipped with Type 1 and Type 3 generators. Different types of fault will be applied to the transmission line to analyze the fault condition with wind penetration.

Chapter 2 describes the most commonly used impedance-based fault location methods and their applications on power networks with conventional power sources. A

transmission line connecting two equivalent sources will be simulated on RTDS to validate the effectiveness of fault location estimation. Chapter 3 develops wind turbine model equipped with Type 1 squirrel-cage induction generator and Type 3 doubly-fed induction generator including the control strategies. Chapter 4 simulates a transmission line connecting equivalent wind plant on RTDS and applies fault location method to examine the validity of existing methods. Chapter 5 analyzes the impact of wind power integration and summarizes the results.

CHAPTER TWO

IMPEDANCE-BASED FAULT LOCATION METHODS

2.1 Faulted Transmission Line

The one-line diagram of a faulted transmission line is shown in Figure 2.1. The transmission line connects source S and source R at each terminal equipped with IED. V_s and V_R are the measured terminal voltages. I_s and I_R are the measured current from each terminal. Z_L represents the impedance of the entire line. When a fault occurs somewhere on the line with total length L, the distance from terminal S to the fault location is defined as m. Consequently, the distance from terminal R to the fault location is defined as $L - m$. The voltage and total fault current at the fault location is named as V_F and I_F.

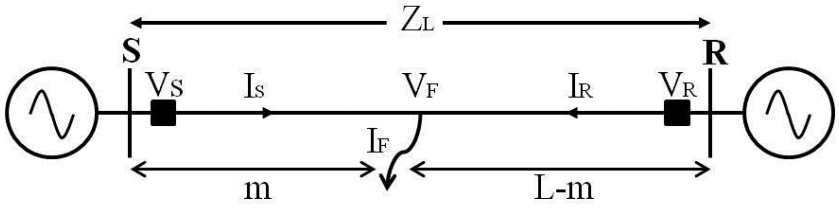

Figure 2.1 – One-line diagram of a faulted transmission line

2.2 One-end Positive-sequence-reactance Method

One-end positive-sequence-reactance method is based on the symmetrical component model of the transmission line. It is assumed that the transmission line is ideally transposed and the phase wires have equal spacing. This results in the equal mutual coupling between phases. The principle of positive-sequence-reactance method can be explained by using fault analysis for a single-line-to-ground fault. Figure 2.2 gives

the symmetrical component circuit model of an A-phase-to-ground fault on the line at a distance m from the sending end.

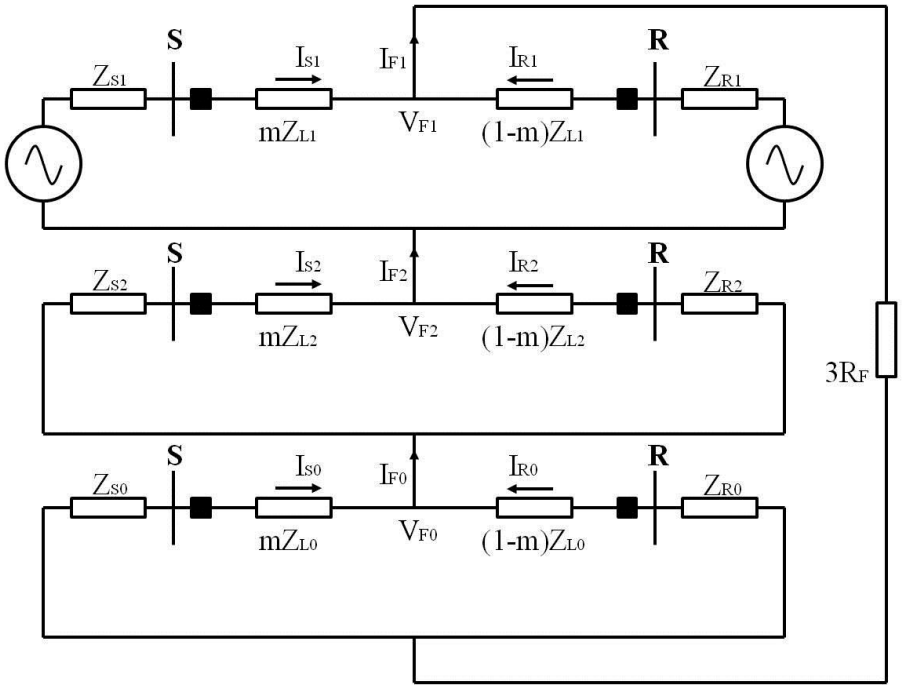

Figure 2.2 – Symmetrical component circuits for A-G fault

The voltage drop from the sending terminal to the fault location can be expressed as:

$$V_{S1} = mZ_{L1}I_{S1} + V_{F1} \tag{2.1}$$

$$V_{S2} = mZ_{L2}I_{S2} + V_{F2} \tag{2.2}$$

$$V_{S0} = mZ_{L0}I_{S0} + V_{F0} \tag{2.3}$$

The summation of the three equations results in:

$$V_{Sa} = mZ_{L1}I_{S1} + mZ_{L2}I_{S2} + mZ_{L0}I_{S0} + V_{Fa} \tag{2.4}$$

Since Z_{L1}, Z_{L2} is assumed to be equal and $I_{S1} = I_{S2} = I_{S0} = \frac{1}{3}I_F$ for A-G fault, $V_{Fa} = R_F I_F$. Equation (2.4) can be rewritten as:

$$V_{Sa} = mZ_{L1}[I_{Sa} + kI_{S0}] + R_F I_F \tag{2.5}$$

Where factor $k = \frac{Z_{L0} - Z_{L1}}{Z_{L1}}$

The voltage and current V_S and I_S is defined as

$$V_S = V_{Sa} \tag{2.6}$$

$$I_S = I_{Sa} + kI_{S0} \tag{2.7}$$

So equation (2.5) can be expressed as

$$V_S = mZ_{L1}I_S + R_F I_F \tag{2.8}$$

The selection of V_s and I_s depends on the fault type, as given in Table 2.1.

Table 2.1 – Selection of measurements for different fault types

Fault Type	V_s	I_s
A-G	V_a	$I_a + k \cdot I_0$
B-G	V_b	$I_b + k \cdot I_0$
C-G	V_c	$I_c + k \cdot I_0$
A-B or A-B-G	V_{ab}	I_{ab}
B-C or B-C-G	V_{bc}	I_{bc}
C-A or C-A-G	V_{ca}	I_{ca}
A-B-C or A-B-C-G	Any of $V_{ab},\ V_{bc},\ V_{ca}$	Any of $I_{ab},\ I_{bc},\ I_{ca}$

The apparent reactance measured at terminal S can be obtained by dividing equation (2.8) by I_s

$$\frac{V_S}{I_S} = mZ_{L1} + R_F \frac{I_F}{I_S} \tag{2.9}$$

To compensate the effect of fault resistance, only the imagery part of equation (2.9) is computed.

$$Im(\frac{V_S}{I_S}) = m \cdot Im(Z_{L1}) + Im(R_F \frac{I_F}{I_S}) \tag{2.10}$$

If complex number I_f and I_s have the same phase angle or R_F is negligible, we will obtain,

$$m = \frac{Im\,(V_s/I_s)}{X_{L1}} \tag{2.11}$$

2.3 One-end Takagi Method

The Takagi method introduced superposed current I_{sup} to eliminate the effect of power flow on fault location accuracy. Therefore, this method assume constant current load model and requires both pre-fault and post-fault data.

$$I_{sup} = I_s - I_{pre} \tag{2.12}$$

Where

I_{pre} is the pre-fault current.

If we multiply equation (2.8) by the conjugate of I_{sup} and extracting the imaginary part, we will obtain,

$$Im\left(V_s \cdot I_{sup}^*\right) = m \cdot Im\left(Z_{L1} \cdot I_s \cdot I_{sup}^*\right) + Im(R_F \cdot I_F \cdot I_{sup}^*) \tag{2.13}$$

If complex number I_F and I_{sup} have the same angle or R_F is negligible, we will obtain,

$$m = \frac{Im\left(V_s \cdot I_{sup}^*\right)}{Im\left(Z_{L1} \cdot I_s \cdot I_{sup}^*\right)} \tag{2.14}$$

2.4 Two-end Negative-sequence Method

Two-end negative-sequence method uses data at both terminals of the transmission line. By using negative-sequence component, the effects of pre-fault power flow and fault resistance are eliminated. Unlike one-end methods, negative-sequence

method requires source impedance to perform fault location estimation. Figure 2.2 shows the negative sequence circuit of a faulted transmission line.

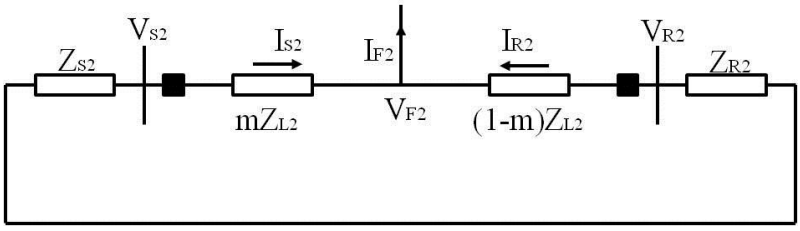

Figure 2.3 – Negative-sequence circuit of a faulted transmission line

At source S,

$$V_{F2} = -I_{S2} \cdot (Z_{S2} + m \cdot Z_{L2}) \tag{2.15}$$

At source R,

$$V_{F2} = I_{R2} \cdot [Z_{R2} + (1 - m) \cdot Z_{L2}] \tag{2.16}$$

By equalizing equation (2.15) and (2.16), we can obtain,

$$I_{R2} = I_{S2} \cdot \frac{Z_{S2} + m \cdot Z_{L2}}{Z_{R2} + (1-m) \cdot Z_{L2}} \tag{2.17}$$

Taking the magnitude of both sides and simplifying the equation, a quadratic equation can be obtained to calculate the fault location estimation m.

2.5 Two-end Three Phase Impedance Matrix Method

Instead of using the symmetrical component model, a fault location method based on the three phase line impedance matrix has been developed. This method is not only applicable to transmission lines, but also distribution feeders. Using Figure 2.1 as the one-line diagram, the voltage at two terminals of the line can be expressed as:

At source S,

$$V_{sabc} = m \cdot Z_{Labc} \cdot I_{sabc} + V_{fabc} \tag{2.18}$$

At source R,

$$V_{rabc} = (1 - m) \cdot Z_{Labc} \cdot I_{rabc} + V_{fabc} \tag{2.19}$$

Where

$V_{sabc} = \begin{bmatrix} V_{sa} \\ V_{sb} \\ V_{sc} \end{bmatrix}$ is the three phase terminal voltage measured at source S,

$I_{sabc} = \begin{bmatrix} I_{sa} \\ I_{sb} \\ I_{sc} \end{bmatrix}$ is the three phase terminal current measured at source S,

$V_{rabc} = \begin{bmatrix} V_{ra} \\ V_{rb} \\ V_{rc} \end{bmatrix}$ is the three phase terminal voltage measured at source R,

$I_{rabc} = \begin{bmatrix} I_{ra} \\ I_{rb} \\ I_{rc} \end{bmatrix}$ is the three phase terminal current measured at source R,

$Z_{Labc} = \begin{bmatrix} Z_{aa} & Z_{ab} & Z_{ac} \\ Z_{ba} & Z_{bb} & Z_{bc} \\ Z_{ca} & Z_{cb} & Z_{cc} \end{bmatrix}$ is the three phase line impedance matrix

$V_{fabc} = \begin{bmatrix} V_{fa} \\ V_{fb} \\ V_{fc} \end{bmatrix}$ is the three-phase voltage at the fault location.

Subtracting equation (2.18) from (2.19), we can obtain,

$$V_{sabc} - V_{rabc} + Z_{Labc} \cdot I_{rabc} = m \cdot Z_{Labc}(I_{sabc} + I_{rabc}) \tag{2.20}$$

V_{sabc}, I_{sabc}, V_{rabc}, I_{rabc} are measured quantities and Z_{Labc} is known if line configuration data is available. Let

$$Y = V_{sabc} - V_{rabc} + Z_{Labc} \cdot I_{rabc} \tag{2.21}$$

$$D = Z_{Labc}(I_{sabc} + I_{rabc}) \tag{2.22}$$

Equation (2.20) becomes equation (2.23), which contains three complex equations and six real equations.

$$Y = m \cdot D \tag{2.23}$$

Least-square estimation can be applied to determine the only unknown parameter m.

2.6 System Simulation on Real-time Digital Simulator

The real-time digital simulator (RTDS) is a combination of computer hardware and software designed for power system electromagnetic transient simulation and analysis. Figure 2.4 shows the basic architecture of RTDS.

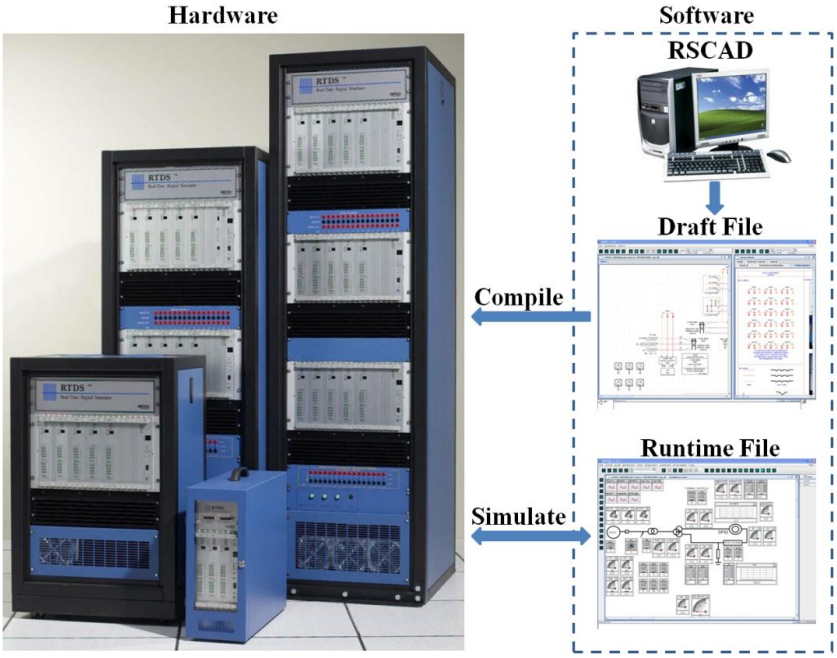

Figure 2.4 – RTDS hardware and software

The RTDS hardware consists of one or many module units called racks. Each rack contains communication cards and processor cards. Communication cards allow communication between racks. The purpose of processor cards is to provide mathematical computations and network solutions for the power and control system

components. There are three types of processor cards, the Giga Processor Card (GPC), the Triple Process Card (3PC) and the RISC Processor Card (RPC) [33]. A typical configuration of the processor cards is using GPC to solve the network and/or compute components and the 3PC to run the software which represents the power and control circuits in real-time.

The RTDS software is a graphic user interface called RSCAD. It allows the user to build power and control system components in a draft file and then compile it. If no error is encountered, the user is ready to run a simulation in a runtime file and analyze simulation results.

Figure 2.5 shows a 230kV transmission line connecting two electric power equivalent sources is simulated using RTDS.

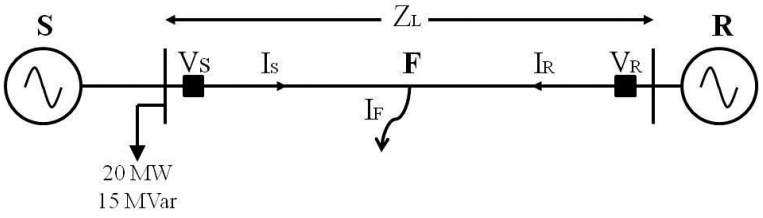

Figure 2.5 – Simulation system one-line diagram

The electric power grid is represented by an equivalent source at terminal S and R with source data as shown in Table 2.2.

Table 2.2 – Source impedance data

Terminal	S	R
Positive-sequence impedance	$10\angle 85^\circ$	$5\angle 80^\circ$
Negative-sequence impedance	$10\angle 85^\circ$	$5\angle 80^\circ$
Zero-sequence impedance	$15\angle 85^\circ$	$7.5\angle 80^\circ$

The transmission line length is 30 miles and has the line impedance data as given in Table 2.3.

Table 2.3 – Transmission line impedance data

Sequence	Resistance (ohms/mile)	Reactance (ohms/mile)
Positive-sequence	0.0031	0.0186
Negative-sequence	0.0031	0.0186
Zero-sequence	0.0093	0.0559

The line impedance per kilometer can be expressed in the form of symmetrical component in matrix notation.

$$Z_{L012} = \begin{bmatrix} 0.0093 + j0.0559 & 0 & 0 \\ 0 & 0.0031 + j0.0186 & 0 \\ 0 & 0 & 0.0031 + j0.0186 \end{bmatrix} \text{ (ohms/mile)}$$

Since one of the fault location methods uses *abc* phase line impedance, the line impedance in the form of symmetrical component is transformed using matrix T,

$$T = \begin{bmatrix} 1 & 1 & 1 \\ 1 & a^2 & a \\ 1 & a & a^2 \end{bmatrix}$$

Where $a = e^{j\frac{2\pi}{3}}$

$$Z_{Labc} = \begin{bmatrix} 0.0083 + j0.05 & 0.0033 + j0.02 & 0.0033 + j0.02 \\ 0.0033 + j0.02 & 0.0083 + j0.05 & 0.0033 + j0.02 \\ 0.0033 + j0.02 & 0.0033 + j0.02 & 0.0083 + j0.05 \end{bmatrix} \text{ (ohms/mile)}$$

Different types of fault are applied to the transmission line. The location of the fault is selected to be 50% of the total line length and the fault resistance is chosen to be 0Ω, 5Ω, 10Ω, 30Ω, 50Ω, 100Ω to demonstrate the effect to the fault location estimation. The duration of the fault is 0.3 seconds. Figure 2.6 shows the implementation of this simulation system in RSCAD.

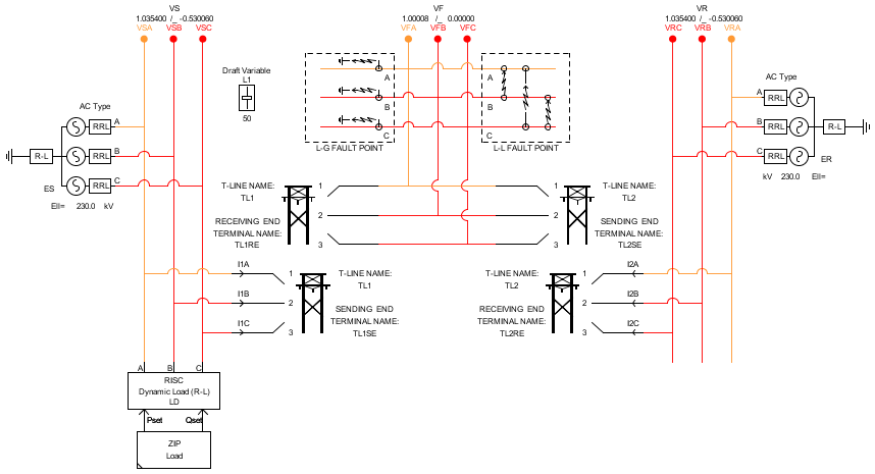

Figure 2.6 – Implementation of simulation system in RSCAD

Fault location estimation results for different types of fault with various fault resistances are collected as listed in Table 2.4 to 2.7. Negative- and zero-sequence components do not apply to three phase fault since it is a balanced fault and system.

Table 2.4 – A-G fault location estimation results

AG fault	Positive X_L Method	Takagi Method	-VE Method	ABC Method
$R_f = 0\Omega$	50.00%	50.00%	49.82%	50.00%
$R_f = 5\Omega$	47.44%	47.09%	49.86%	49.53%
$R_f = 10\Omega$	44.66%	44.11%	49.88%	49.27%
$R_f = 30\Omega$	38.52%	38.21%	49.89%	49.14%
$R_f = 50\Omega$	15.10%	20.42%	49.89%	49.08%
$R_f = 100\Omega$	-41.24%	-9.59%	49.89%	49.06%

Table 2.5 – B-C fault location estimation results

BC fault	Positive X_L Method	Takagi Method	-VE Method	ABC Method
$R_f = 0\Omega$	49.98%	49.98%	49.79%	50.01%
$R_f = 5\Omega$	47.30%	47.26%	49.80%	51.21%
$R_f = 10\Omega$	44.53%	44.53%	49.82%	51.75%
$R_f = 30\Omega$	31.39%	33.57%	49.88%	52.52%
$R_f = 50\Omega$	15.86%	22.56%	49.89%	52.86%
$R_f = 100\Omega$	-34.47%	-5.27%	49.89%	52.08%

Table 2.6 – B-C-G fault location estimation results

BCG fault	Positive X_L Method	Takagi Method	-VE Method	ABC Method
$R_f = 0\Omega$	50.05%	50.05%	49.73%	49.98%
$R_f = 5\Omega$	44.40%	44.50%	49.80%	51.63%
$R_f = 10\Omega$	38.15%	38.95%	49.86%	51.80%
$R_f = 30\Omega$	6.89%	16.54%	49.89%	51.59%
$R_f = 50\Omega$	-34.91%	-6.15%	49.89%	51.54%
$R_f = 100\Omega$	-189.00%	-64.17%	49.89%	51.52%

Table 2.7 – Three phase fault location estimation results

ABC fault	Positive X_L Method	Takagi Method	-VE Method	ABC Method
$R_f = 0\Omega$	50.08%	50.08%	NA	49.99%
$R_f = 5\Omega$	44.32%	44.29%	NA	50.00%
$R_f = 10\Omega$	37.88%	38.42%	NA	50.00%
$R_f = 30\Omega$	6.45%	15.47%	NA	50.00%
$R_f = 50\Omega$	-35.55%	-7.77%	NA	50.00%
$R_f = 100\Omega$	-190.35%	-67.43%	NA	50.00%

As shown in these tables, for conventional power generation sources, positive-sequence-reactance method and Takagi method have an increasing fault location estimation error with the increasing of fault resistance, while negative-sequence method and three-phase impedance method are immune to fault resistance and maintain accurate results.

CHAPTER THREE

WIND FARM MODEL

3.1 Wind Turbine Generating System

A wind farm usually includes tens or hundreds of wind towers. Each tower can be treated as an independent electric power generation unit. In terms of electrical point of view, a typical wind generation unit consists of wind turbine, generating system and control system. Wind turbine extracts the power from wind and output mechanical torque through gearbox to drive the generator. Figure 3.1 shows the general structure of a wind power generation system.

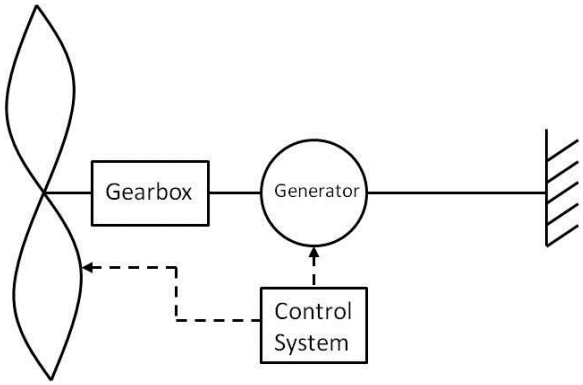

Figure 3.1 – Wind power generation systems

Horizontal-axis three-blade wind turbines are the most commonly manufactured turbine in today's wind energy market and will be used through this thesis if not otherwise stated. A wind turbine extracts wind energy from the swept area of the rotor disc and drives an electrical generator through rotor shaft and gearbox. The power extracted from the wind turbine is given by the equation 3.1:

$$P = \frac{1}{2} C_P(\lambda, \beta) \rho A V^3 \tag{3.1}$$

Where C_P is power coefficient; ρ is air density (approx. 1.225kg/m^3); A is the swept area of rotor blades; V is the wind speed.

Power coefficient C_P is one of the two parameters that describe the performance of a wind turbine. By Betz limit, C_P can never be more than 59.3 percent for any fluid turbine, which indicates that the maximum power a wind turbine can extract is 59.3 percent of the power from air stream. The other parameter is defined as tip speed ratio and is given by equation (3.2)

$$\lambda = \frac{\omega R}{V} \tag{3.2}$$

Where ω is the rotational speed of rotor; R is the radius to tip of rotor.

Wind turbine operates either at fixed speed or variable speed. Fixed-speed induction generator-based wind turbines are simple and cheap. They can be directly connected to the grid. Capacitors are used to improve the power factor of induction generator. In recent years, technology has switched from fixed-speed to variable speed for the advantages that variable-speed wind turbines have less mechanical stress and noise, better power quality and system efficiency, and are able to operate effectively over a wide range of wind speed.

Akhmatov [34] stated that there is no mutual interaction if the wind turbine is equipped with induction generator and the converter is well tuned. Therefore, a wind plant can be modeled as a reduced equivalent. In the next three sections, reduced wind plant model using squirrel-cage induction generator (SCIG), wound-rotor induction generator (WRIG) and doubly-fed induction generator (DFIG) are introduced as they are

the models that used in the simulation system to demonstrate the validity of fault location methods.

3.2 Type 1 SCIG Wind Plant Model

A Type 1 wind turbine generator using SCIG is shown in Figure 3.2. Shunt capacitor is installed to excite the generator and compensate the reactive power consumed by the induction generator. This model includes pitch angle control so that the generator can deliver rated power output to the grid at fixed rotational speed.

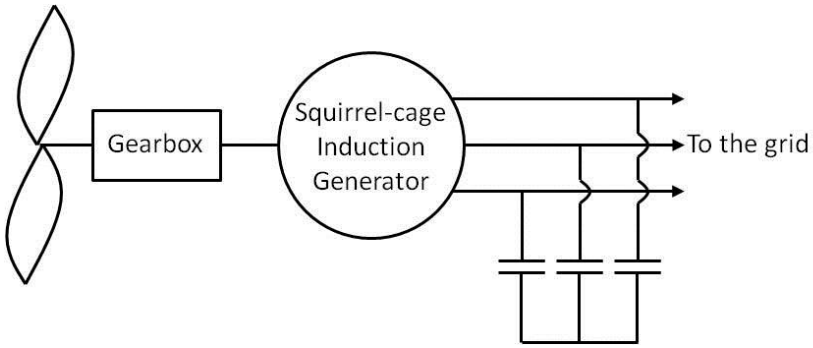

Figure 3.2 – Squirrel-cage induction generator

The wind plant equipped with SCIG is simulated by an equivalent reduced model. Three SCIGs were connected in parallel to the power plant substation and then to the grid through a step-up transformer and transmission line, as shown in Figure 3.3.

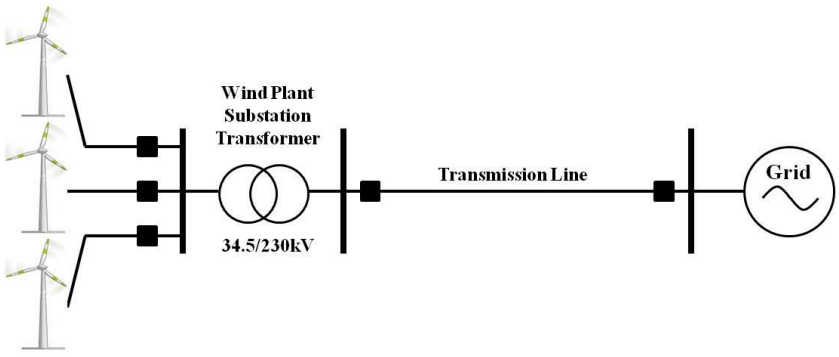

Figure 3.3 – Type 1 Wind plant model

The rated power of the wind turbine is 1.65MW. The cut-in and rated wind speed is 3.5 m/s and 13 m/s respectively. Figure 3.4 shows the relationship between power coefficient C_P and tip speed ratio λ, blade pitch angle β of the wind turbine.

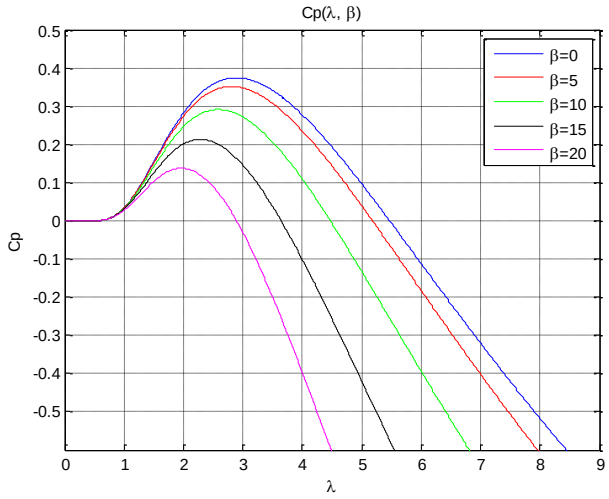

Figure 3.4 – Power coefficient curve of the SCIG wind turbine

Each wind turbine is controlled by the adjustment of the pitch angle for starting. The wind turbine implementation in RSCAD is shown in Figure 3.5.

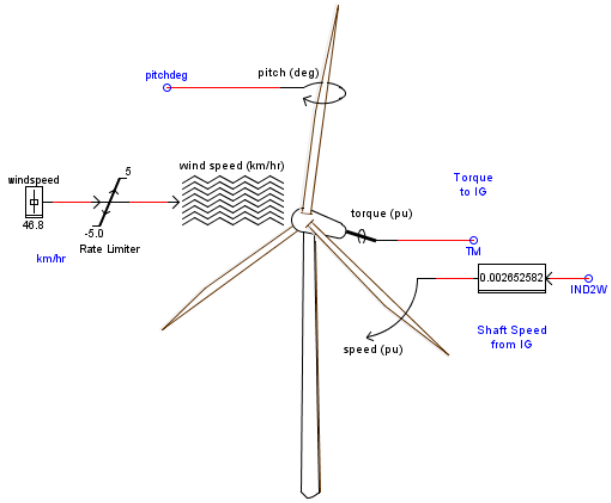

Figure 3.5 – Implementation of wind turbine in RSCAD

When the turbine is first started, the pitch angle is set to minimum value zero to provide maximum starting torque. Once the turbine is started, it drives the induction generator to rotate and the speed of the turbine shaft increases. After the turbine is rotating over a certain speed, the pitch angle control begins to adjust and decelerate the turbine so that it will not exceed the speed limit.

The turbine is considered to be successfully started if the shaft speed maintains slightly above the synchronous speed. In this situation, the induction generator starts to excite with the existence of shunt capacitor bank.

The capacitor bank includes five separate units. Each unit provides 140 kVar reactive power. Four units are required to excite the induction generator and the remains can be used to improve the power factor at the generator output terminal. Table 3.1 gives the parameters of the induction generator in the SCIG model on a 1.808MVA and 0.69kV base.

Table 3.1 – Induction generator parameters (On 1.808MVA, 0.69kV base)

Rating (MVA)	1.808
Stator Voltage (L-L)	0.69kV
Rated Slip (pu)	0.00625
Stator Resistance (pu)	0.0077
Stator Reactance (pu)	0.0697
Rotor Resistance (pu)	0.0062
Rotor Reactance (pu)	0.0834
Magnetizing Reactance (pu)	3.454

Once the induction generator is successfully started and excited, a voltage synchronization check between the generator side and the grid side is performed before

the breaker is closed to connect the wind plant to the grid. Figure 3.6 shows the synchronization check in RSCAD.

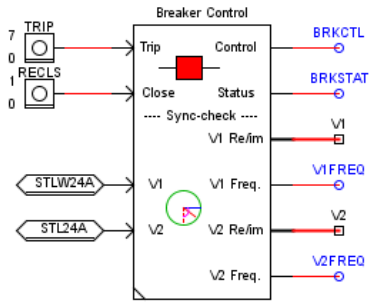

Figure 3.6 – Synchronization check for wind plant

After the voltage of the wind plant and the grid are synchronized, the breaker is closed and the wind power is delivered to the grid. The three Type 1 wind turbines are started and connected to the grid one after another. Figure 3.7 explains the general control logic of wind turbine starting.

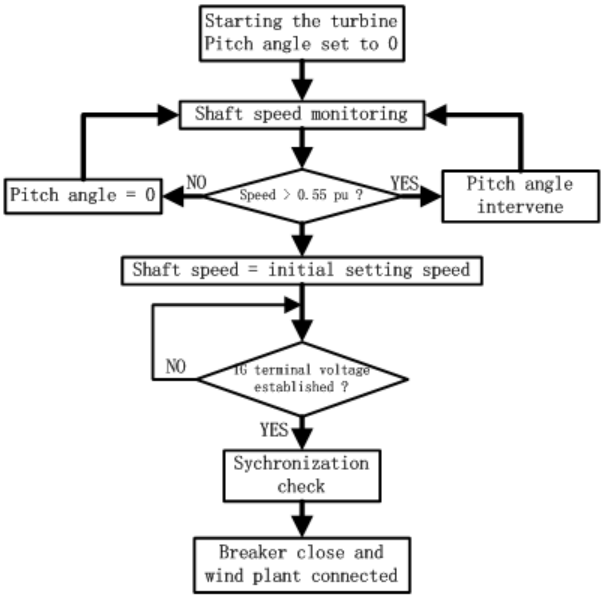

Figure 3.7 – Flow chart of wind turbine starting control logic

Due to the variable speed of the wind, pitch angle control must be active to keep the induction generator operating at nominal speed. It uses a simple linear PI control method. When wind speed is between nominal speed and cut-out speed, the power output of the wind generator is maintained at rated value 1.65MW. Figure 3.8 shows the pitch angle control scheme. PI controller parameters are adjusted to provide satisfactory performance based on the case.

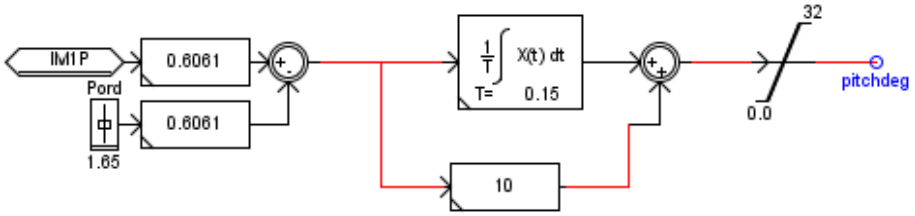

Figure 3.8 – Pitch angle control of SCIG

Although fixed-speed wind turbine generators are simple and robust, they are not able to optimally extract the power from the wind due to the limit of operation speed. For this reason, variable-speed wind turbines are employed more commonly in commercial wind power plants.

3.3 Type 2 WRIG Wind Plant Model

Type 2 wind turbine generator is similar to Type 1 except that a WRIG is used. The rotor resistance can be variable to adjust the generator slip in an allowable range. Therefore, Type 2 generator is able to operate at a variable slip up to 5% of the synchronous speed. Figure 3.9 shows the WRIG used in RSCAD.

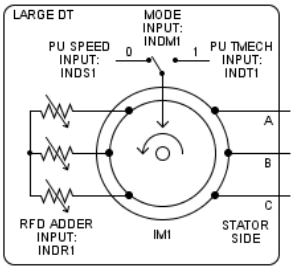

Figure 3.9 – WRIG in RSCAD

The Type 2 wind plant model is built as same as the Type 1 wind plant model in Figure 3.3. All three Type 2 wind turbine generators have the same technical parameters. They are started and connected to the grid in the same way. The only difference in this model is that pitch angle control is replaced by variable slip control when the slip is between rated value and 5% of the synchronous speed during normal operation. Figure 3.10 explains the control logic in flow chart.

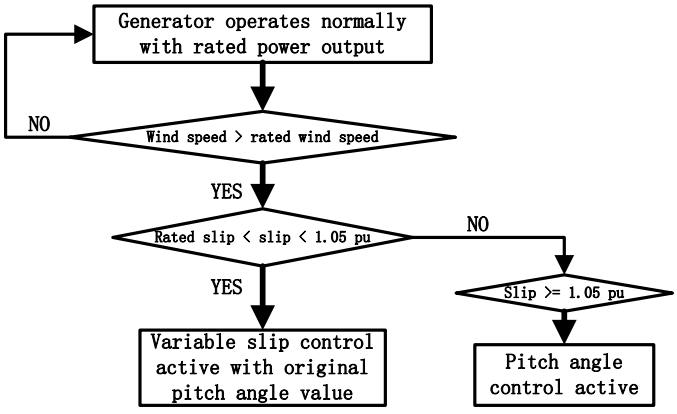

Figure 3.10 – Flow chart of variable slip control logic

In this way, the generator speed can be adjusted in an allowable range without the interference of pitch angle control while still deliver rated power output.

Compared with Type 1 wind turbine generator, the advantage of Type 2 wind turbine generator is being able to provide variable slip if wind speed exceeds rated speed.

This helps the turbine to extract power from wind optimally. However, both Type 1 and Type 2 wind plants require reactive power to excite the generator and improve the power factor. The requirement of active and advanced power control leads to an increasing share of Type 3 wind turbine generator in commercial wind power plant market.

3.4 Type 3 DFIG Wind Plant Model

A wind turbine equipped with DFIG is a various-speed type generating system, as shown in Figure 3.11. A back-to-back converter is connected across the stator and rotor side of the induction generator. The real and reactive power coming out of the generating system can be controlled to achieve optimal power output. Control schemes such as pitch angle control, converter vector control are then applied to maintain rated power output.

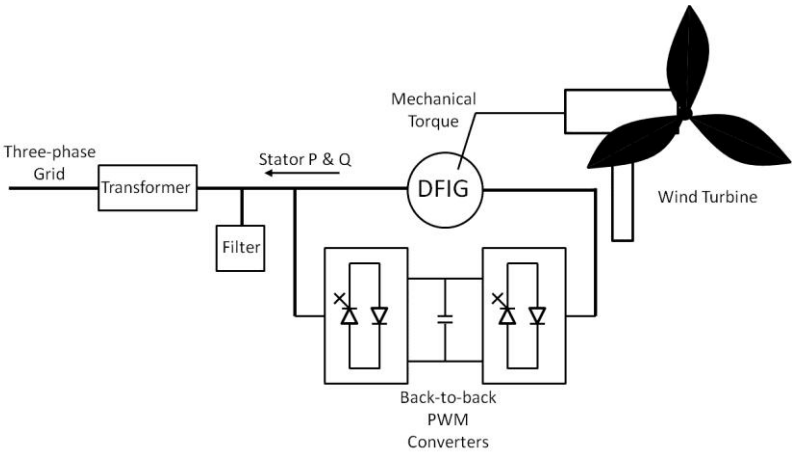

Figure 3.11 – Structure of DFIG

DFIG consists of a wounded rotor induction generator (WRIG) and a bidirectional back-to-back PWM voltage source converter (VSC). Byeon [35] implemented the DFIG structure with Scherbius circuit and vector-control scheme in RTDS. Real wind speed signal was obtained from an anemometer and sent to RTDS through an analogue input card. The performance of the DFIG proved the validity of the model. A DFIG-equipped

wind farm with a static synchronous compensator (STATCOM) was modeled in RTDS [36]. Steady state voltage regulation and three-phase short circuit grid fault simulation were performed to study short-term voltage stability. The results have shown that the STATCOM is able to provide dynamic voltage support and reestablish the voltage shortly after grid fault for fault-ride-through requirement.

The DFIG wind turbine model used in the simulation has rated power 2MW. The cut-in and rated wind speed is 6 m/s and 12m/s respectively. Figure 3.12 shows the relationship between power coefficient C_P and tip speed ratio λ, blade pitch angle β of the wind turbine.

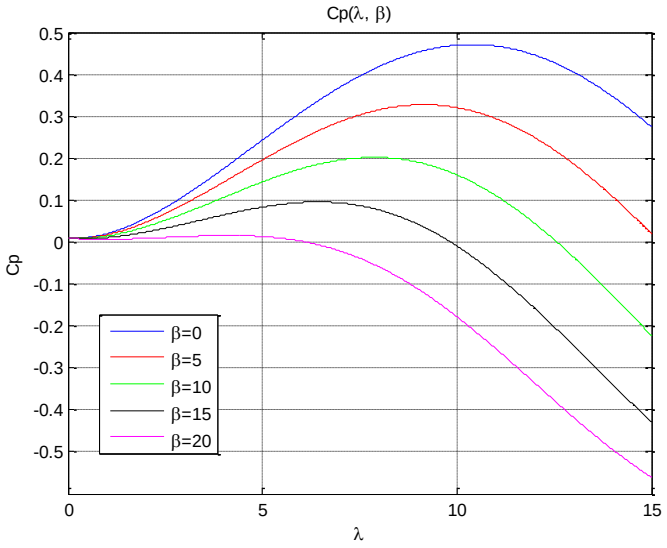

Figure 3.12 – Power coefficient curve of the DFIG wind turbine

Figure 3.13 gives a clear illustration of the technical performance of a variable-speed wind turbine with base wind speed 12m/s, and nominal mechanical output power 2MW in per unit value. When the nominal speed of the wind turbine is 1.0 pu, the generator speed is 1.2 pu.

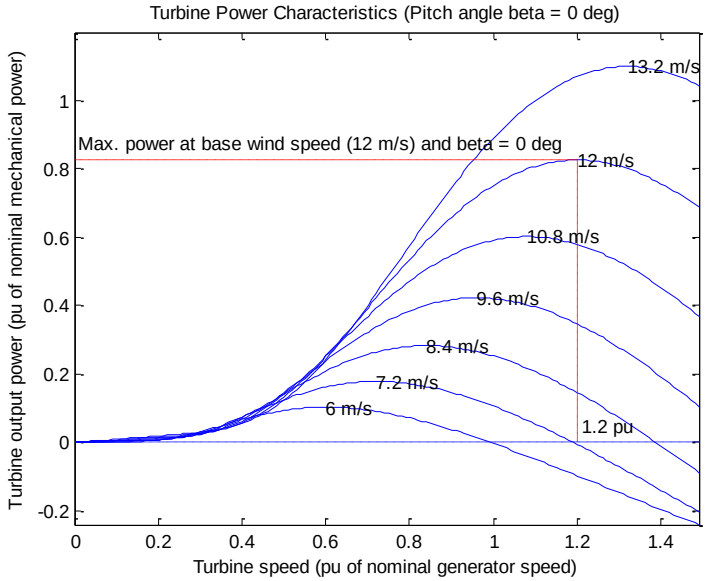

Figure 3.13 – DFIG wind turbine power characteristics

The implementation of the wind turbine in RSCAD is shown in Figure 3.14.

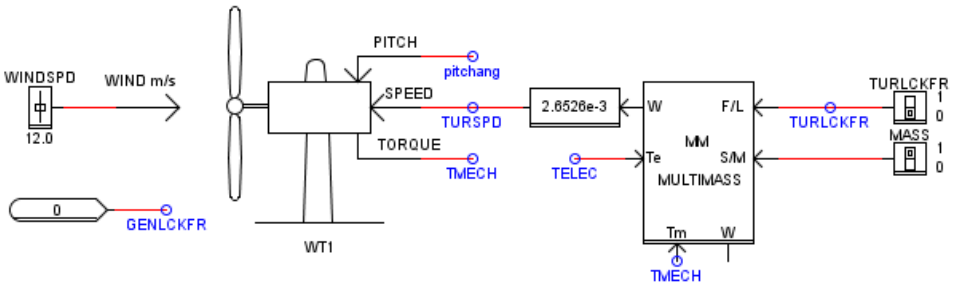

Figure 3.14 – Implementation of DFIG wind turbine in RSCAD

The generator parameters of the DFIG are listed in Table 3.2.

Table 3.2 – DFIG parameters (On 2.2MVA, 0.69kV base)

Rating (MVA)	2.2
Stator Voltage (L-L)	0.69kV
Stator Resistance (pu)	0.0046
Stator Reactance (pu)	0.1020
Rotor Resistance (pu)	0.0060
Rotor Reactance (pu)	0.1109
Magnetizing Reactance (pu)	4.3480

Figure 3.15 illustrates how DFIG is connected with the back-to-back converter and transfer power to the grid through a three-phase three-winding unit transformer in small time step network in RSCAD. The voltage is stepped up from 0.69kV to 34.5kV.

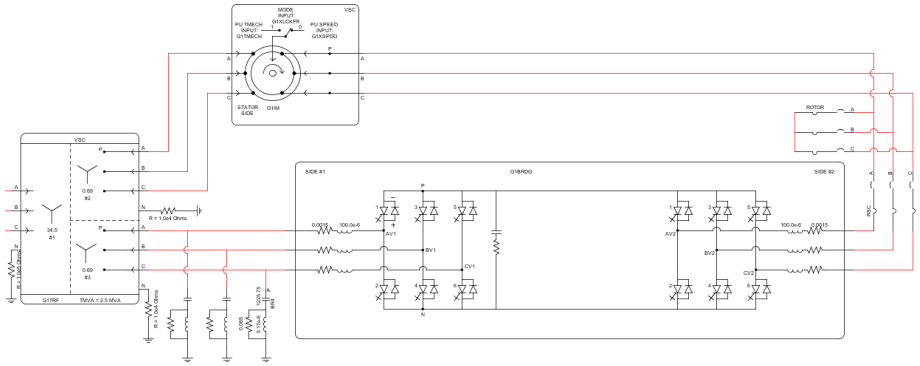

Figure 3.15 – DFIG structure in RSCAD

The DFIG model is implemented in the small time step regime and connected to 3 single phase interface transformers, as shown in Figure 3.16. The interface transformers are the bridge between large time networks and small time networks. They are used to change scaling in terms of rating and current so that a single wind generator can represent an entire wind farm.

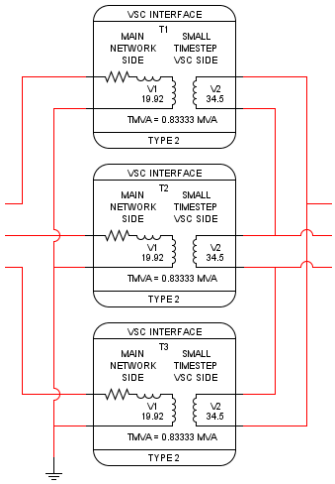

Figure 3.16 – Interface transformer in RSCAD

Once the DFIG model and interface transformers are connected, they must be contained in a small time step box so that the large time network can access it. Figure 3.17 shows the model in large time step network.

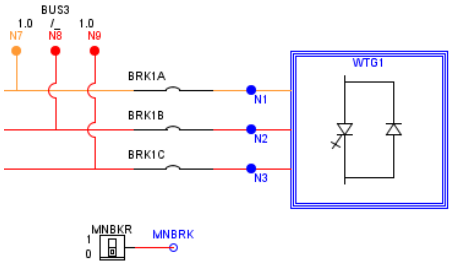

Figure 3.17 – Large time-step connection in RSCAD

Pena [27] and Salman [29] discussed a Scherbius scheme in DFIG structure. The Scherbius circuit consists of two back-to-back PWM converters. One is connected to the rotor side of the DFIG to regulate the real and reactive power coming out of the stator, referred as rotor-side converter (RSC). The other is connected to the grid side of the DFIG to keep the DC-link voltage constant and regulate the reactive power coming out from the back-to-back converter, referred as grid-side converter (GSC).

Vector-control strategy is applied to both RSC and GSC. The control strategy is based on the direct-quadrature (*d*-*q*) axis model of the induction machine. An operating induction machine can be assumed to have symmetrical air gap. Therefore, the theory of rotating fields and *d*-*q* axis model is applied to analyze the operating principle of an induction generator. A detailed review of transformation between reference frames and equation derivation is given in [37, 38] to help understand the *d*-*q* representation of an induction machine.

The purpose of the RSC control is to achieve desire stator power output by independent control of rotor d-q axis current. The instantaneous three-phase power S_{sabc}, rotor voltage V_{rabc}, rotor currents i_{rabc}, stator voltages V_{sabc} and stator currents i_{sabc} are transformed into *d-q* axis frame so that all elements are computed in the stator flux-oriented reference frame. After the transformation, the stator flux linkage equations are:

$$\lambda_{sq} = L_s i_{sq} + L_o i_{rq} \tag{3.3}$$

$$\lambda_{sd} = L_s i_{sd} + L_o i_{rd} \tag{3.4}$$

The rotor flux linkage equations are:

$$\lambda_{rq} = L_r i_{rq} + L_o i_{sq} \tag{3.5}$$

$$\lambda_{rd} = L_r i_{rd} + L_o i_{sd} \tag{3.6}$$

The stator voltage equations are:

$$V_{sq} = \frac{d}{dt}\lambda_{sq} + \omega_e \lambda_{sd} + R_s i_{sq} \tag{3.7}$$

$$V_{sd} = \frac{d}{dt}\lambda_{sd} - \omega_e \lambda_{sq} + R_s i_{sd} \tag{3.8}$$

Where ω_e designates synchronous speed (rad/s)

The rotor voltage equations are:

$$V_{rq} = \frac{d}{dt}\lambda_{rq} + (\omega_e - \omega_r)\lambda_{rd} + R_r i_{rq} \tag{3.9}$$

$$V_{rd} = \frac{d}{dt}\lambda_{rd} - (\omega_e - \omega_r)\lambda_{rq} + R_r i_{rd} \tag{3.10}$$

Where

ω_r designates rotor angular speed (rad/s)

The power equations are:

$$P_s = \frac{3}{2}(V_{sd} i_{sd} + V_{sq} i_{sq}) \tag{3.11}$$

$$Q_s = \frac{3}{2}(V_{sq} i_{sd} - V_{sd} i_{sq}) \tag{3.12}$$

The *d*-axis of the reference frame is aligned to the stator flux linkage, which makes λ_{sd} a constant value and $\lambda_{sq} = 0$. Therefore, $V_{sd} = 0$ if we substitute λ_{sq} and λ_{sd} in equation (3.8) and neglect the stator resistance, which results in

$$P_s = \frac{3}{2} V_{sq} i_{sq} \tag{3.13}$$

$$Q_s = \frac{3}{2} V_{sq} i_{sd} \tag{3.14}$$

Also, the substitution of $\lambda_{sq} = 0$ in equation (3.3) will give us

$$i_{sq} = -\frac{L_o}{L_s} i_{rq} \tag{3.15}$$

$$i_{ms} = \frac{\lambda_s}{L_o} = \frac{\lambda_{sd}}{L_o} \tag{3.16}$$

Where

i_{ms} is the stator magnetizing current, which is a constant value

L_s, L_r, L_o are the stator, rotor and magnetizing inductance of the induction generator.

Now we substitute λ_{sd} of equation (3.14) in equation (3.4) and we will obtain:

$$i_{sd} = \frac{L_o}{L_s}(i_{ms} - i_{rd}) \tag{3.17}$$

From equation (3.13) and (3.15), we can see that the stator *d*-*q* axis current can be expressed by the rotor *d*-*q* axis current. Substitution of i_{sq} and i_{sd} in equation (3.11) and (3.12) will give us

$$P_s = -\frac{3}{2}\frac{L_o}{L_s} V_{sq} i_{rq} \tag{3.18}$$

$$Q_s = \frac{3}{2} V_{sq} \frac{L_o}{L_s} (i_{ms} - i_{rd}) \tag{3.19}$$

Where V_{sq} is a constant value due to $V_{sd} = 0$.

This derivation results in a decoupled relationship between stator real and reactive power P_s, Q_s and *d-q* axis rotor current i_{rd}, i_{rq}. Thus, an independent control of the stator power is achieved by rotor current regulation. The substitution of equation (3.13) in (3.3) and (3.15) in (3.4) will result in

$$\lambda_{rq} = (L_r - \frac{L_o^2}{L_s}) i_{rq} \tag{3.20}$$

$$\lambda_{rd} = \frac{L_o^2}{L_s} i_{ms} + (L_r - \frac{L_o^2}{L_s}) i_{rd} \tag{3.21}$$

Now we substitute equation (3.18) and (3.19) in (3.9) and (3.10),

$$v_{rq} = R_r i_{rq} + \sigma L_r \frac{d}{dt} i_{rq} + \omega_{slip} (L_m i_{ms} + \sigma L_r i_{rd}) \tag{3.22}$$

$$v_{rd} = R_r i_{rd} + \sigma L_r \frac{d}{dt} i_{rd} - \omega_{slip} \sigma L_r i_{rq} \tag{3.23}$$

$$\sigma = 1 - \frac{L_o^2}{L_s L_r} \tag{3.24}$$

$$L_m = \frac{L_o^2}{L_s} \tag{3.25}$$

$$\omega_{slip} = \omega_e - \omega_r \tag{3.26}$$

Figure 3.18 shows the overall vector control scheme of the RSC. With desired stator power output P_s, Q_s, the reference values of i_{rd}, i_{rq} can be determined. Linear proportional and integration (PI) control is designed to generate voltage control signals v_{rd}^* and v_{rq}^* that drive the rotor-side sinusoidal PWM (SPWM) module. The voltage signals are compensated by the cross coupling terms.

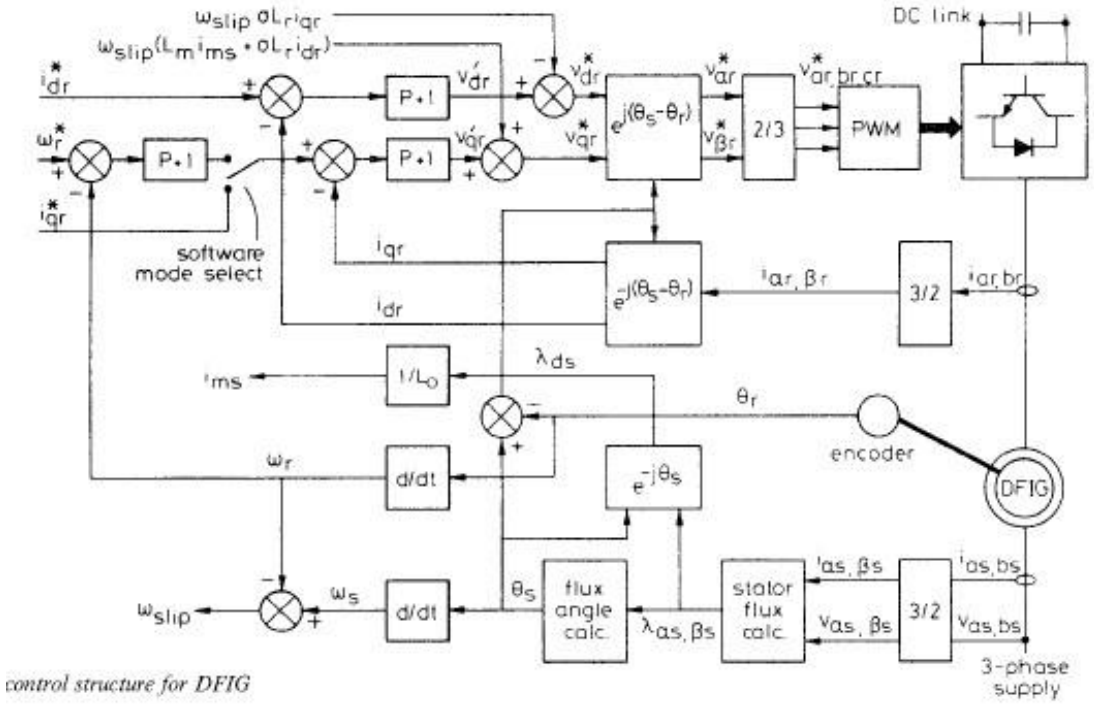

Figure 3.18 – Control scheme of RSC

The first step of the vector control scheme for RSC is flux angle calculation. The relationship between the stator flux linkage, voltage and current can be expressed in matrix notation as:

$$\begin{bmatrix} v_{sa} \\ v_{sb} \\ v_{sc} \end{bmatrix} = \frac{d}{dt}\begin{bmatrix} \lambda_{sa} \\ \lambda_{sb} \\ \lambda_{sc} \end{bmatrix} + \begin{bmatrix} R_s & 0 & 0 \\ 0 & R_s & 0 \\ 0 & 0 & R_s \end{bmatrix}\begin{bmatrix} i_{sa} \\ i_{sb} \\ i_{sc} \end{bmatrix} \tag{3.27}$$

A phase locked loop (PLL) is applied to obtain the instantaneous stator flux angle. Figure 3.19 shows the implementation of PLL in RSCAD.

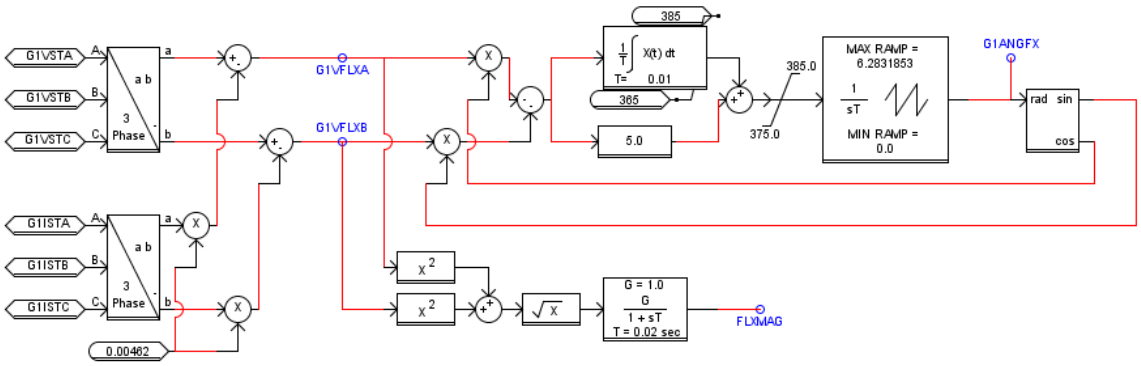

Figure 3.19 – Calculation of stator flux angle

Figure 3.20 shows the reference frame transformation applied to the rotor current. The difference of stator flux angle and rotor angle is the transformation angle.

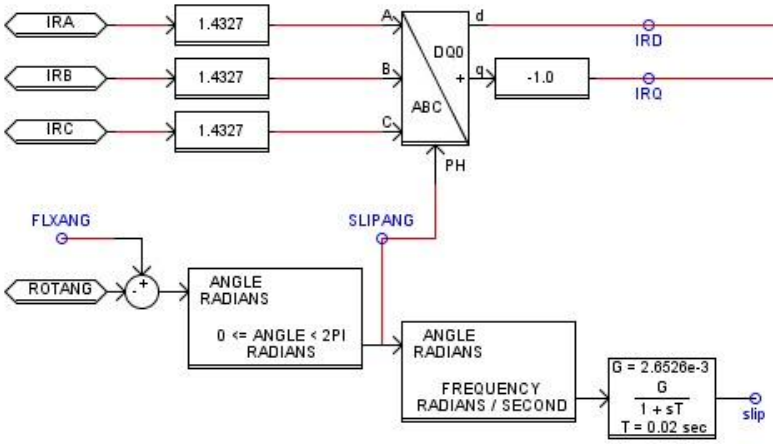

Figure 3.20 – Reference frame transformation of rotor current

The results of the transformation are i_{rd} and i_{rq}, which represent the actual value of the *d*-*q* axis rotor current.

The next step is to regulate the *d*-*q* axis rotor current. Based on equation (3.22) and (3.23), Figure 3.21 shows how it is done through PI control. The actual value of *d*-*q* axis rotor current is compared with the reference value to generate error signal. The errors are processed by the PI controller. Compensation terms are added to the output of

the PI controller to generate voltage reference signal. The purpose of PI control is to reduce the error in the loop so that reference value of i_{rd} and i_{rq} is obtained to achieve desired power output.

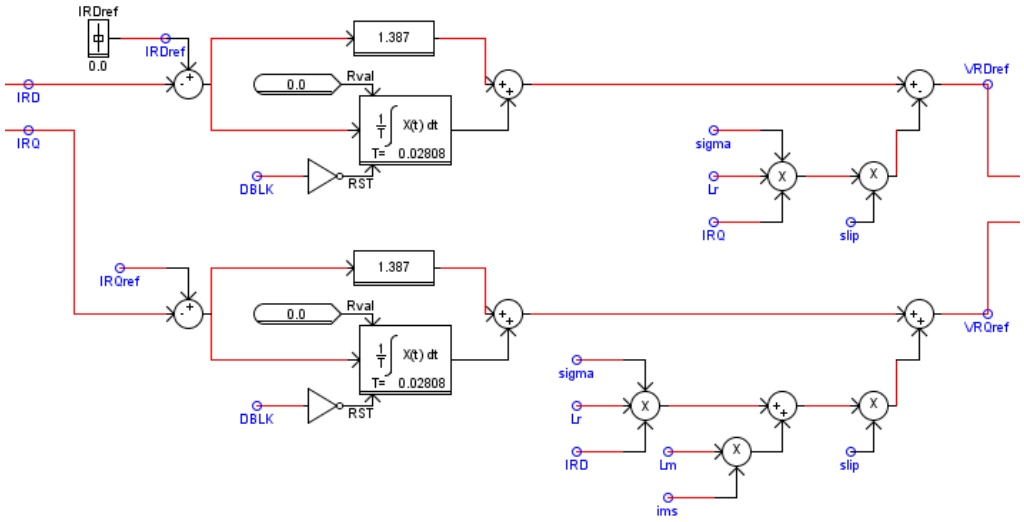

Figure 3.21 – Rotor current regulation

The selection of PI controller parameters is based on satisfactory performance of the DFIG model.

After the voltage reference signals are generated, they are then transformed from d-q axis back to abc phase to drive SPWM, as shown in Figure 3.22.

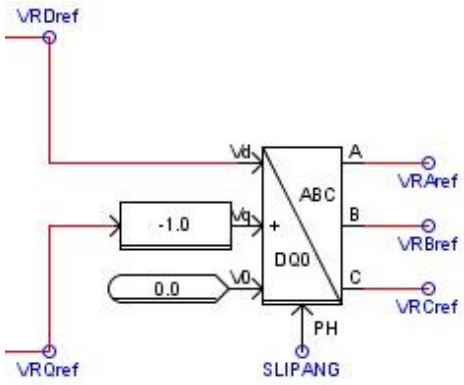

Figure 3.22 – Inverse transformation from *d-q* to *abc*

Reference value i_{rq}^{*} is obtained by optimal power calculation. Since the torque and the *d*-*q* axis current in per unit has the relationship as

$$T_e = -\frac{1}{2} L_m i_{ms} i_{rq} \tag{3.28}$$

The torque value is calculated based on the speed of the rotor. As mentioned in the previous section, the nominal speed of the generator is 1.2 times the nominal speed of the wind turbine. Therefore, the speed is converted to the turbine base. Similarly, the optimal power is converted from generator base to turbine base. Figure 3.23 gives the optimal power calculation.

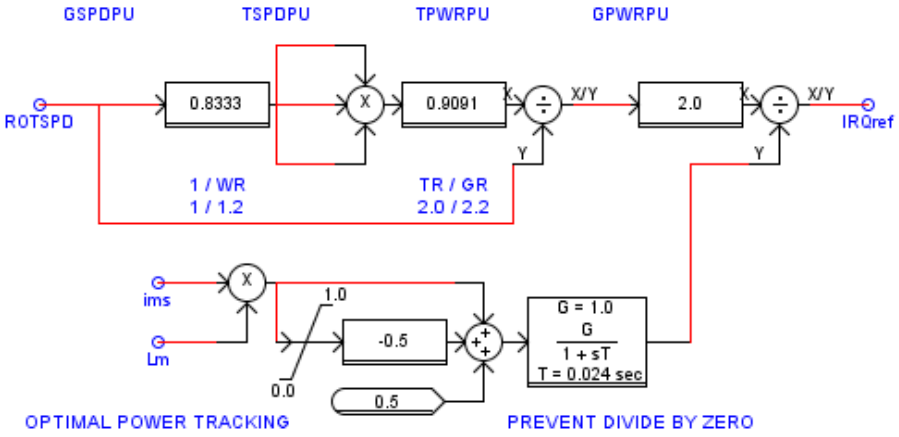

Figure 3.23 – Optimal power calculation

Pitch angle control for wind turbine equipped with DFIG is similar to the wind turbine equipped with SCIG, as shown in Figure 3.24.

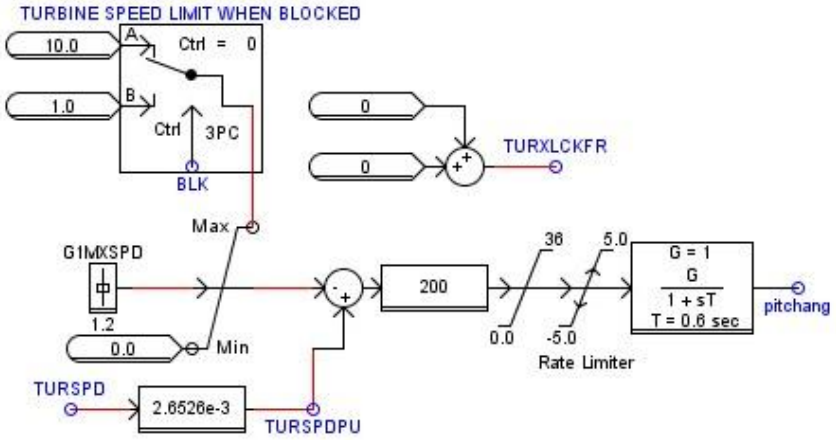

Figure 3.24 – DFIG pitch angle control

The objective of GSC is to maintain the DC-link voltage constant regardless of the rotor power flow direction. On the grid side, the instantaneous three-phase GSC currents i_{gabc}, voltages v_{gabc} are transformed into *d-q* axis frame so that all elements are computed in the stator flux-oriented reference frame. Figure 3.25 shows the electrical model of the GSC.

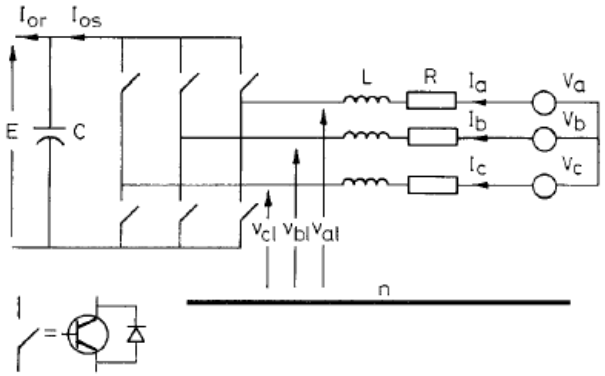

Figure 3.25 – Electrical structure of GSC

Voltage equations at the grid side can be written as

$$V_g^{abc} = \frac{d}{dt}\lambda_g^{abc} + R_g^{abc} i_g^{abc} \tag{3.29}$$

Applying the transformation onto the synchronous reference frame, we will obtain

$$V_{gd} = R_g i_{gd} + L_g \frac{d}{dt} i_{gd} - \omega_e L_g i_{gq} \tag{3.30}$$

$$V_{gq} = R_g i_{gq} + L_g \frac{d}{dt} i_{gq} + \omega_e L_g i_{gd} \tag{3.31}$$

Instead of aligning the d-axis of the reference frame to the stator flux linkage vector as in RSC control, GSC control aligns the *d*-axis to the stator voltage vector, which makes V_{gd} a constant value and $V_{gq} = 0$. Therefore, a similar equation like (3.11) can be written as

$$P_g = E i_{os} = \frac{3}{2} V_{gd} i_{gd} \tag{3.32}$$

$$Q_g = \frac{3}{2} V_{gd} i_{gq} \tag{3.33}$$

$$v_{gd} = \frac{m_1}{2\sqrt{2}} E \tag{3.34}$$

$$C \frac{dE}{dt} = i_{os} - i_{or} \tag{3.35}$$

Figure 3.26 shows the overall vector control scheme of GSC. In normal operation, the reference value of the GSC reactive power Q_g^* is set to zero to be reactively neutral, which results in the *q*-axis reference current value of the GSC i_{gq} to be zero. The linear PI control here is designed to generate voltage control signals V_{gd} and V_{gq} that drive the grid side PWM module. The voltage signals are compensated by the cross coupling terms.

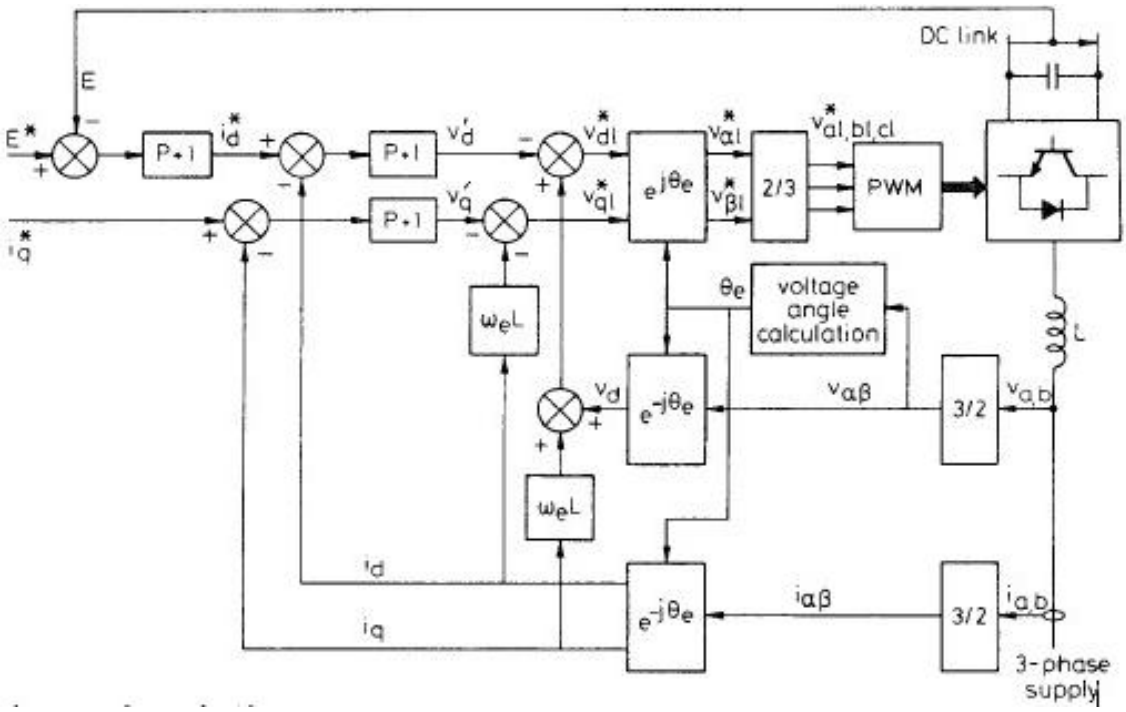

Figure 3.26 – Control scheme of GSC

The first step of the vector control scheme for GSC is to transform the grid side current i_g from *abc* to *d-q* axis, as shown in Figure 3.27. The transformation angle is equal to grid side voltage angle.

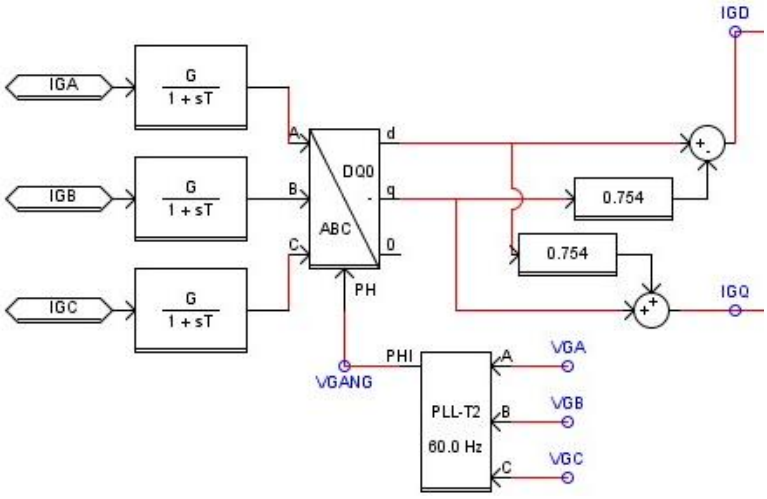

Figure 3.27 – Reference frame transformation of grid side current

The nominal voltage across the capacitor of the back-to-back converter E is set to be 1.5kV DC. This DC voltage can be controlled by i_{gd}, as given in the equation (3.36).

$$Ei_{os} = \frac{3}{2} v_{gd} i_{gd} \tag{3.36}$$

The reference value i_{gd}^{*} is obtained by generating the error between actual and nominal voltage and process through PI control. The parameter of the PI controller is selected by satisfactory performance for this case. Figure 3.28 shows the control implementation in RSCAD.

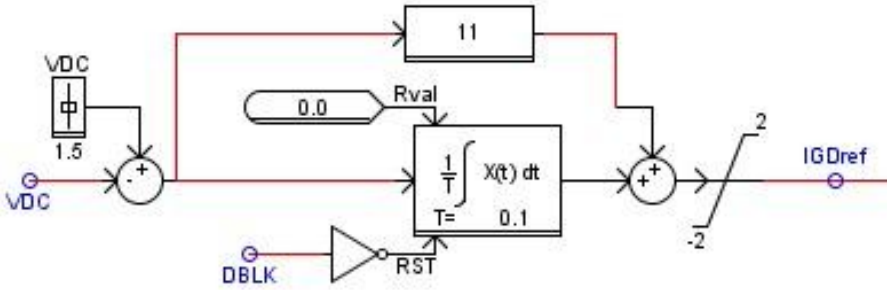

Figure 3.28 – DC-link voltage control

Based on equation (3.30) and (3.31), Figure 3.29 shows how *d-q* axis grid side current is regulated through PI control. The actual value of *d-q* axis current is compared with the reference value to generate error signal. The errors are processed by the PI controller. Compensation terms are added to the output of the PI controller to generate voltage reference signal. The purpose of PI control is to reduce the error in the loop so that reference value of i_{gd} and i_{gq} is obtained to achieve desired power output. The selection of PI controller parameters is based on satisfactory performance of the DFIG model.

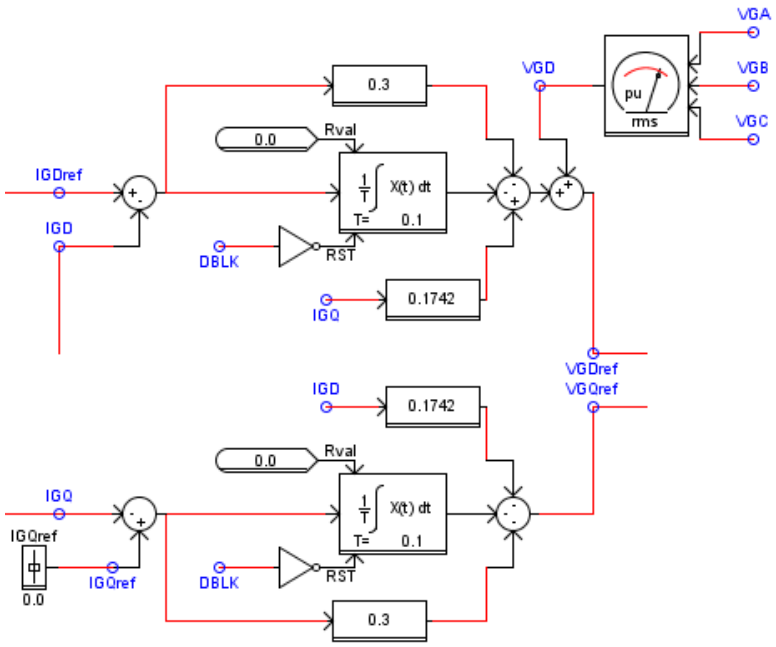

Figure 3.29 – GSC current regulation

Type 3 wind turbine generators are employed by many new commercial wind power plants in the recent years. The independent control of real and reactive power output improves the performance of a wind plant and provides a promising future for wind power integration to the existing electric power grid.

With all three types of wind turbine generators illustrated in this chapter, the impact of these renewable energy systems to the conventional fault location method can be examined and analyzed by simulation using RTDS. In Chapter 4, the simulation system and the corresponding results will be discussed.

CHAPTER FOUR

SYSTEM SIMULATION AND RESULTS

4.1 SCIG Wind Farm Simulation

In this chapter, three types of wind farms are simulated in the system described in Chapter 2. The equivalent source at terminal R is replaced by wind farm plants equipped with SCIG, WRIG and DFIG respectively to validate the effectiveness of the existing fault location methods. Figure 4.1 shows the simulation system in RSCAD.

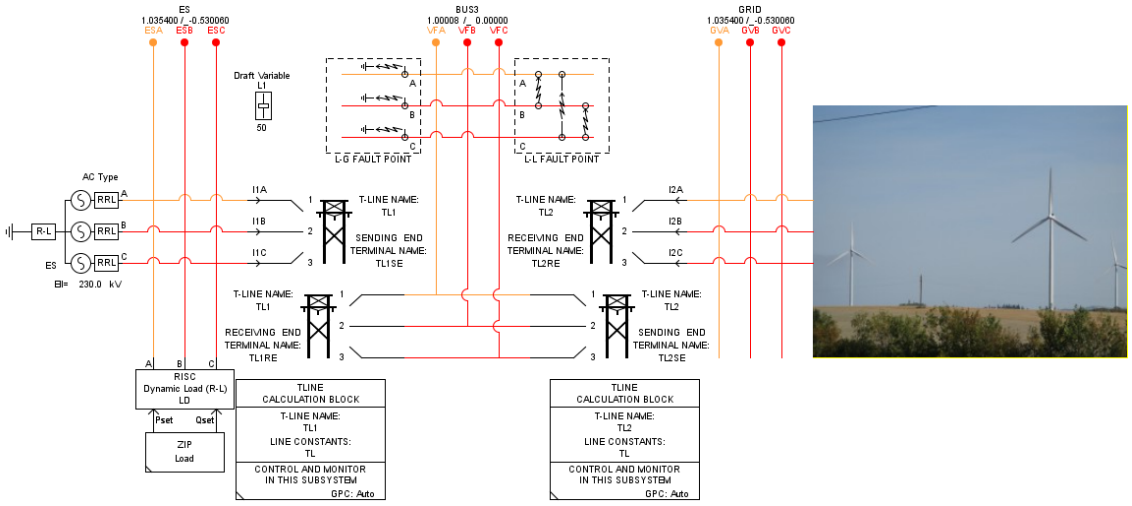

Figure 4.1 – SCIG wind farm simulation in RSCAD

In the simulation system, voltage and current signals are captured by PMU at both terminals of the transmission line. The PMU is configured to capture data in a rate of 60 frames per second. Figure 4.2 shows the PMU data of the voltage at the sending end of the line during single-line-to-ground as an example. Magnitude and angle values are separately illustrated for each phase voltage and current.

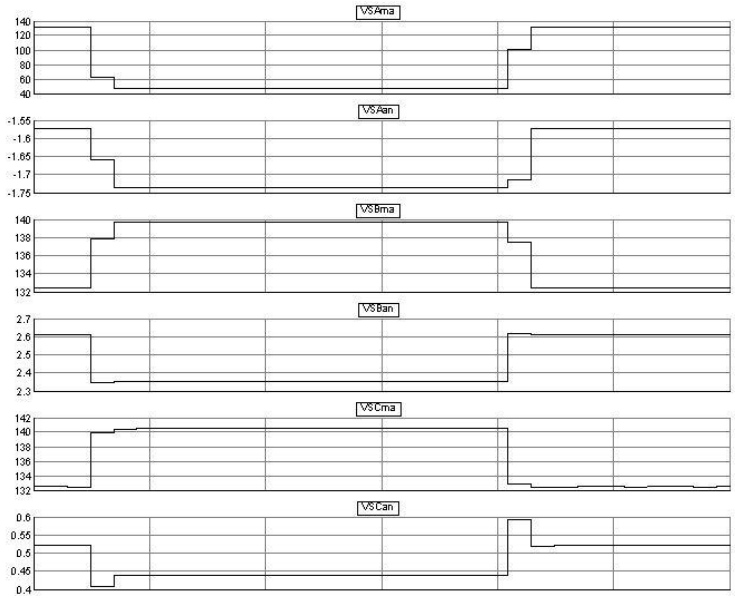

Figure 4.2 – Example of PMU data captured for fault location estimation

The PMU data are exported from RSCAD and then imported to MATLAB for fault location estimation. The algorithm of positive-sequence-reactance method and Takagi method utilize voltage and current data only at the sending terminal.

For negative-sequence method, the negative-sequence impedance of the wind farm is required to estimate the fault location. It is derived based on the symmetrical component model, as shown in Figure 4.3.

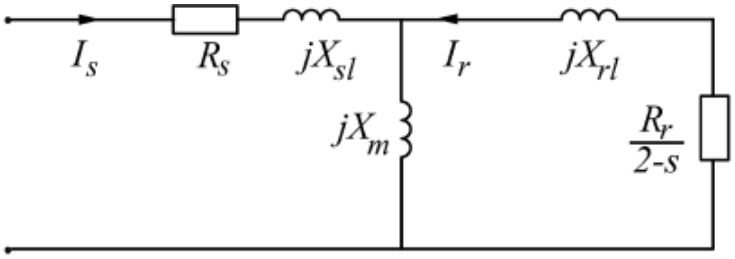

Figure 4.3 – Negative-sequence equivalent circuit of SCIG

The negative-sequence impedance of a single SCIG can be expressed as

$$Z_{neg} = R_s + jX_s + jX_m//(\frac{R_r}{2-s} + jX_r) \quad (4.1)$$

where s is the slip of the induction generator.

Since the slip of the induction generator is less than 2% during normal conditions, we can assume that the slip value does not affect the negative-sequence impedance, which results in:

$$Z_{neg} \cong R_s + jX_s + jX_m//(\frac{R_r}{2} + jX_r) \quad (4.2)$$

The substitution of the parameters given in Table 3.1 into equation (4.2) gives $Z_{neg} = 0.0107 + j0.1511$ in per unit value on the base of 1.808MVA and 0.6kV.

Three-phase impedance method uses three-phase voltage and current data from both terminals of the line. Therefore, PMU data captured by both terminals will be used to validate the fault location accuracy.

The fault is applied at the middle point of the transmission line and lasts for 0.2 seconds. The results of the fault location estimation are listed in Table 4.1 through Table 4.4 as shown below. A-G fault stands for single-line-to-ground fault on phase A, B-C fault stands for line-to-line fault on phase B and C, B-C-G fault stands for double-line-to-ground fault on phase B and C.

Table 4.1 – SCIG wind farm fault location estimation for A-G fault

AG fault	+VE Reactance Method	Takagi Method	-VE Method	ABC Method
$R_f = 0\Omega$	50.01%	50.01%	45.62%	50.02%
$R_f = 5\Omega$	50.04%	49.98%	44.98%	50.95%
$R_f = 10\Omega$	50.07%	49.95%	44.39%	52.29%
$R_f = 30\Omega$	50.25%	49.79%	43.47%	53.91%
$R_f = 50\Omega$	50.57%	49.66%	43.47%	54.15%
$R_f = 100\Omega$	51.73%	49.28%	43.43%	54.28%

Table 4.1 shows the fault location estimation for A-G with different fault resistance. With the fault location at the middle of the transmission line, Figure 4.4 represents the fault location estimation error for SCIG-based wind power plant during A-G fault.

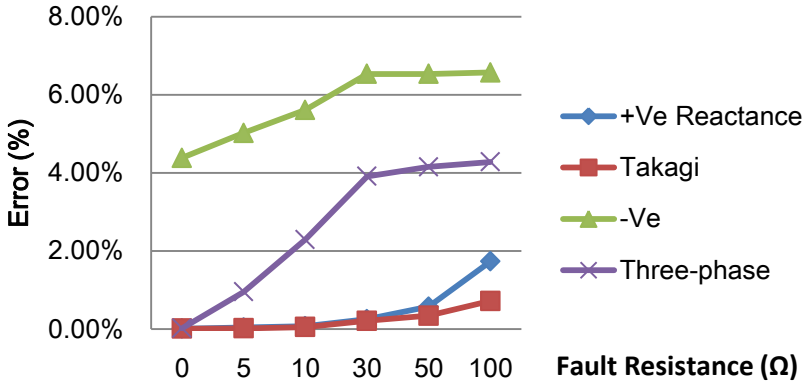

Figure 4.4 – SCIG wind farm fault location estimation error for A-G fault

Positive-sequence-reactance method gives fault location estimation error of less than 2% and Takagi method less than 1%. Takagi method provides better estimation than positive-sequence-reactance method by considering the pre-fault current.

Negative-sequence method gives fault location estimation with an error of nearly 6% mainly because of the approximation of equivalent negative-sequence impedance required by the algorithm. During a fault condition, it is not practical to obtain an accurate equivalent negative-sequence impedance of a wind farm plant. Therefore, it is expected that this method may provide even worse estimations for the other two type of wind farm plant. In addition, this method does not apply to three-phase fault since no negative-sequence component is involved in a three-phase fault.

It was observed that positive-sequence-reactance method and Takagi method produced good fault location estimation, while negative-sequence method and three-phase impedance method gave less accurate estimation. The reason for this is analyzed by looking at the fault current contribution from the grid and from the wind farm plant. Figure 4.4 shows the fault current captured at both terminals of the line during an A-G fault with a 30 Ω fault resistance. With a different fault resistance, the fault current contribution from the grid follows the same pattern but different magnitude while the fault current contribution from the wind farm plant is found to be similar both in pattern and magnitude.

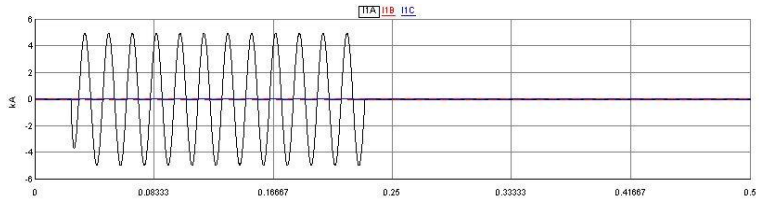

(a) Fault current contribution from the grid terminal

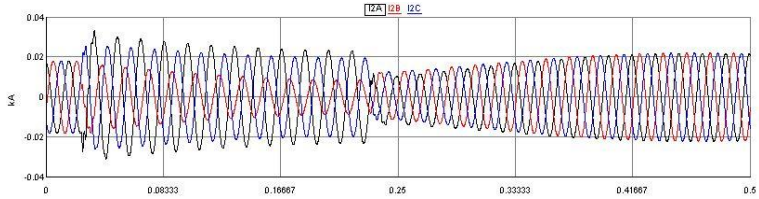

(b) Fault current contribution from the wind plant terminal

Figure 4.5 – SCIG fault current contribution for A-G fault with $R_f = 30\Omega$

As shown in Figure 4.4, the fault current flowing from the grid side terminal is much higher than the current flowing from the wind farm plant. As a matter of fact, the fault current contributed by the wind farm plant is not very different from its pre-fault current. The voltage and current data captured at the grid side terminal plays a major role

in identifying the fault location than the data captured at the wind farm terminal. This is the reason why one-end methods can provide more accurate fault location estimation than two-end methods in this case.

It is also found that the error of the fault location estimation slightly increases with the increase of the fault resistance. This observation indicates that fault resistance still affects the accuracy of one-end method estimation, but the impact is greatly diminished due to the large difference between fault current contributions from both terminals.

Table 4.2 – SCIG wind farm fault location estimation for B-C fault

BC fault	+VE Reactance Method	Takagi Method	-VE Method	ABC Method
$R_f = 0\Omega$	50.06%	50.06%	47.12%	50.05%
$R_f = 5\Omega$	50.03%	49.98%	46.88%	47.90%
$R_f = 10\Omega$	50.05%	49.96%	46.63%	43.98%
$R_f = 30\Omega$	50.17%	49.88%	45.92%	33.44%
$R_f = 50\Omega$	50.34%	49.81%	44.35%	30.07%
$R_f = 100\Omega$	51.07%	49.63%	43.33%	27.71%

Table 4.2 shows the fault location estimation for B-C fault with different fault resistance. Figure 4.6 represents the fault location estimation error for SCIG-based wind power plant during a B-C fault.

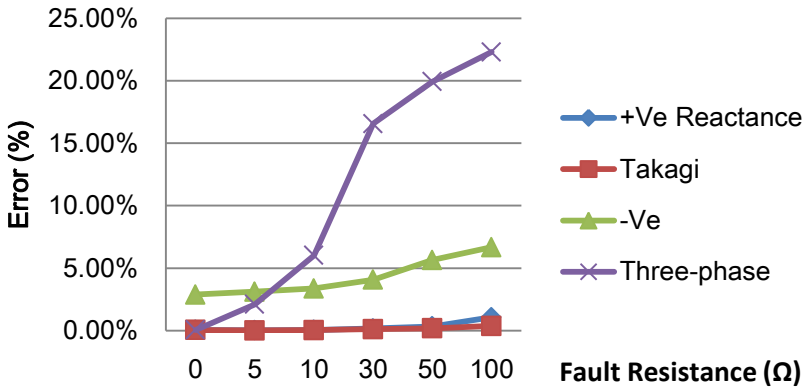

Figure 4.6 – SCIG wind farm fault location estimation error for B-C fault

Positive-sequence-reactance method and Takagi method provides fault location error estimation of nearly 1%. The error of fault location estimation of negative-sequence method is less than 8%, while three-phase impedance method has 22.29% error when the fault resistance is 100 Ω. The possible reason for such a large error for three-phase impedance method is that this method uses least-square estimation based on the voltage and current data captured at both terminals of the line. During fault condition, the current magnitude of the wind farm plant terminal does not change much with the fault resistance. Therefore, the current data captured at that terminal is not able to provide good estimation.

Figure 4.7 shows the fault current captured at both terminals of the line during a B-C fault with a 30 Ω fault resistance.

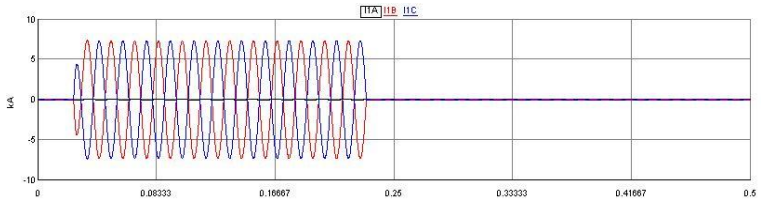

(a) Fault current contribution from the grid terminal

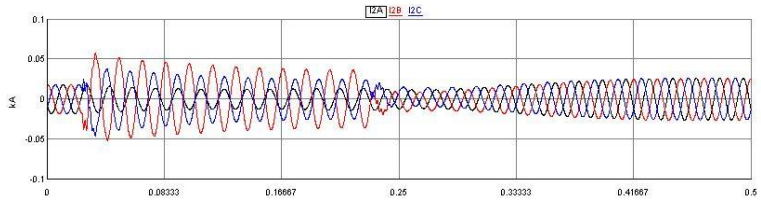

(b) Fault current contribution from the wind plant terminal

Figure 4.7 – SCIG fault current contribution for B-C fault with $R_f = 30\Omega$

The post-fault current contributed from the wind farm plant is twice the magnitude of the pre-fault current. Similar to A-G fault, the fault current contributed from the wind farm plant is much lower than the current from the grid but remains nearly the same with the pre-fault current.

Table 4.3 – SCIG wind farm fault location estimation for B-C-G fault

BCG fault	+VE Reactance Method	Takagi Method	-VE Method	ABC Method
$R_f = 0\Omega$	50.00%	50.00%	48.90%	49.99%
$R_f = 5\Omega$	50.05%	49.96%	48.89%	45.01%
$R_f = 10\Omega$	50.11%	49.92%	48.68%	41.64%
$R_f = 30\Omega$	50.46%	49.74%	48.00%	41.61%
$R_f = 50\Omega$	51.11%	49.59%	45.51%	42.32%
$R_f = 100\Omega$	53.88%	49.16%	42.77%	42.83%

Table 4.3 shows the fault location estimation for B-C-G fault with different fault resistance. Figure 4.8 represents the fault location estimation error for SCIG-based wind power plant during a B-C-G fault.

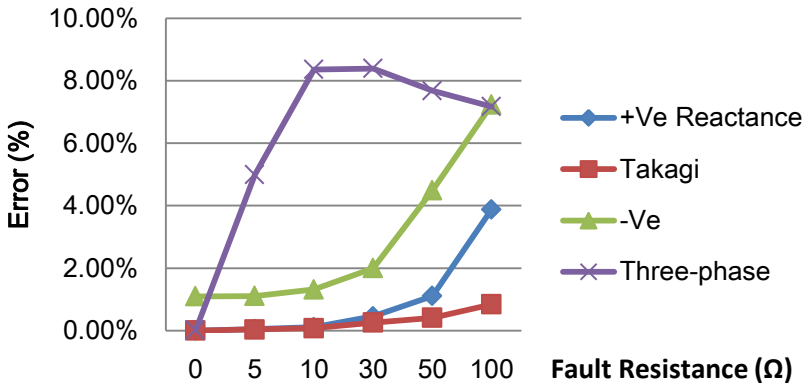

Figure 4.8 – SCIG wind farm fault location estimation error for B-C-G fault

Positive-sequence-reactance method and Takagi method provide fault location estimation errors of less than 4% and 1%. Similar to the previous fault types, positive-sequence-reactance method and Takagi method provides better fault location estimation than negative-sequence method and three-phase impedance method. Figure 4.9 shows the fault current captured at both terminals of the line during a B-C-G fault with a 30 Ω fault resistance.

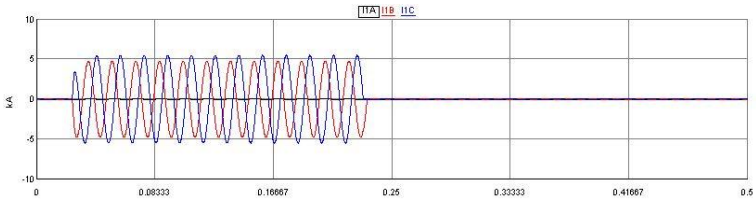

(a) Fault current contribution from the grid terminal

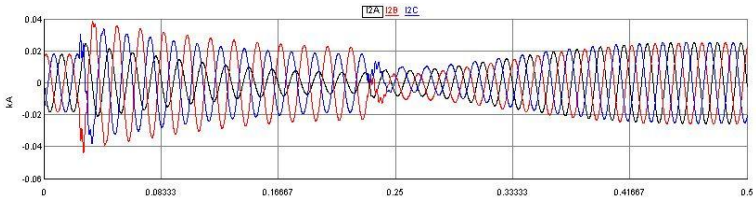

(b) Fault current contribution from the wind plant terminal

Figure 4.9 – SCIG fault current contribution for B-C-G fault with $R_f = 30\Omega$

The post-fault current contributed from the wind farm plant is twice the magnitude of the pre-fault current. Similarly, the fault current contributed from the wind farm plant is much lower than the current from the grid.

Table 4.4 – SCIG wind farm fault location estimation for three-phase fault

ABC fault	+VE Reactance Method	Takagi Method	-VE Method	ABC Method
$R_f = 0\Omega$	50.07%	50.07%	NA	50.02%
$R_f = 5\Omega$	50.05%	49.95%	NA	50.01%
$R_f = 10\Omega$	50.10%	49.89%	NA	50.02%
$R_f = 30\Omega$	50.38%	49.55%	NA	50.02%
$R_f = 50\Omega$	50.99%	49.27%	NA	50.01%
$R_f = 100\Omega$	53.63%	48.51%	NA	50.02%

Table 4.4 shows the fault location estimation for three-phase fault with different fault resistance. Figure 4.10 represents the fault location estimation error for SCIG-based wind power plant during a three-phase fault.

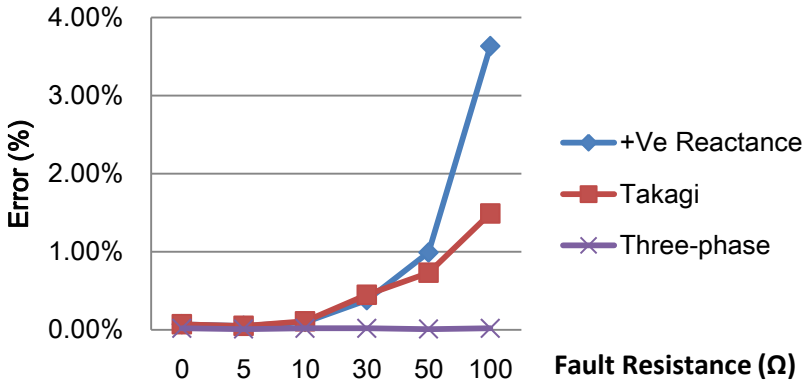

Figure 4.10 – SCIG wind farm fault location estimation error for three-phase fault

Negative-sequence method is not applied to this type of fault because negative-sequence component does not exist during a symmetrical fault. Takagi method provides a slightly better estimation than positive-sequence-reactance method. Figure

4.11 shows the fault current captured at both terminals of the line during a three-phase fault with 30 Ω fault resistance.

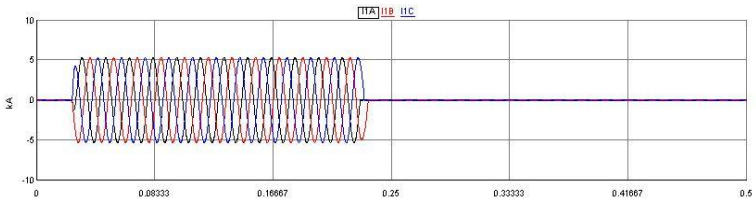

(a) Fault current contribution from the grid terminal

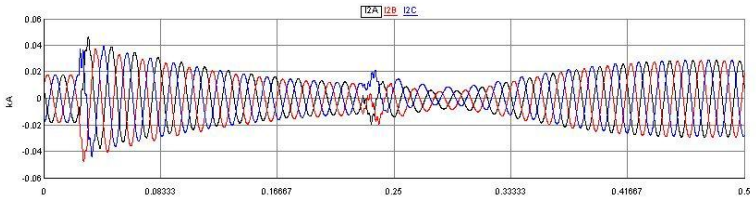

(b) Fault current contribution from the wind plant terminal

Figure 4.11 – SCIG fault current contribution for three-phase fault with $R_f = 30\Omega$

In this symmetrical fault, three-phase impedance method gives more accurate estimation than the one-end methods. The reason is that three-phase impedance method is based on least-square estimation of the available data. For symmetrical fault, the voltage and current data captured at both terminals are also symmetrical. This provides a better estimation than unsymmetrical data during unsymmetrical faults.

4.2 WRIG Wind Farm Simulation

Similar to Type 1 SCIG wind farm, Type 2 WRIG wind farm is simulated using the same system as shown in Figure 4.1. The addition of an external rotor resistance replaces R_r with $R_r + R_{ext}$ in equation (4.2) and gives a new equation (4.3) to calculate the negative-sequence impedance.

$$Z_{neg} = R_s + jX_s + jX_m//(\frac{R_r+R_{ext}}{2-s} + jX_r) \quad (4.3)$$

With the same fault location occurrence and fault time duration, the results of the fault location estimation are listed in Table 4.5 through Table 4.8.

Table 4.5 – WRIG wind farm fault location estimation for A-G fault

AG fault	+VE Reactance Method	Takagi Method	-VE Method	ABC Method
$R_f = 0\Omega$	50.00%	50.00%	38.94%	49.79%
$R_f = 5\Omega$	50.04%	49.99%	39.55%	50.65%
$R_f = 10\Omega$	50.08%	49.97%	38.89%	50.68%
$R_f = 30\Omega$	50.31%	49.92%	38.90%	49.33%
$R_f = 50\Omega$	50.60%	49.82%	38.43%	49.28%
$R_f = 100\Omega$	51.90%	49.83%	37.99%	48.97%

Table 4.5 shows the fault location estimation for A-G fault with different fault resistance. Figure 4.12 represents the fault location estimation error for WRIG-based wind power plant during A-G fault.

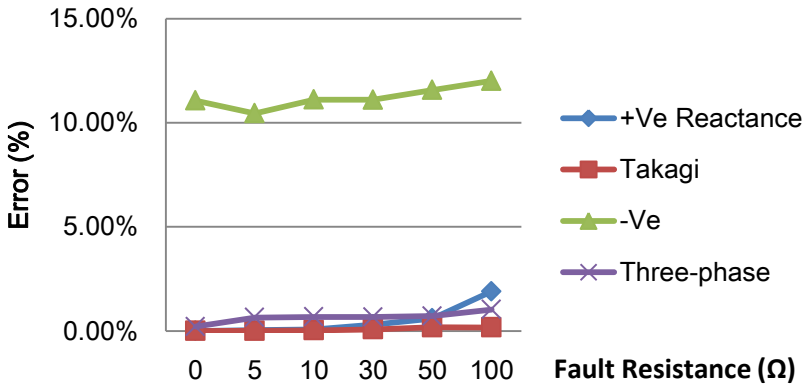

Figure 4.12 – WRIG wind farm fault location estimation error for A-G fault

It is observed that Takagi method provides the most accurate estimation among the four methods with less than 1% error, while negative-sequence method provides estimation error of more than 10%. If we compare the results in Table 4.1 with the results

in Table 4.5, we can see that negative-sequence method applied to WRIG wind farm plant gives a worse estimation than when applied to SCIG wind farm plant. The main reason is the external resistance that added to the rotor winding affects the calculation of the equivalent negative-sequence impedance. During the fault condition, the existence of an external rotor resistance increases the difficulty of determining the negative-sequence impedance.

Figure 4.13 shows the fault current captured at both terminals of the line during a phase A to ground fault with a 30 Ω fault resistance. With a different fault resistance, the fault current contribution from the grid follows the same pattern but different magnitude while the fault current contribution from the wind farm plant is found to be similar both in pattern and magnitude.

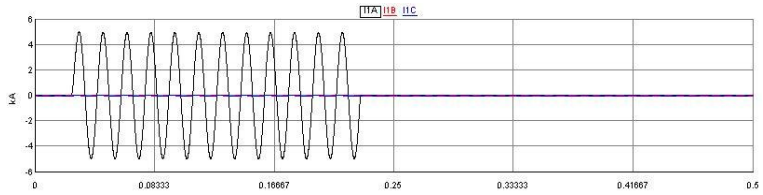

(a) Fault current contribution from the grid terminal

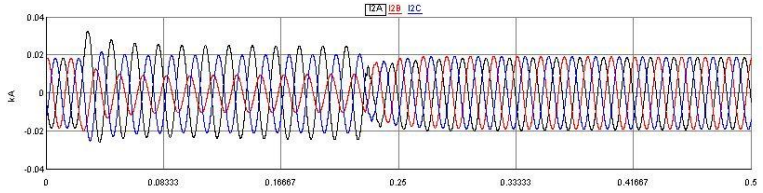

(b) Fault current contribution from the wind plant terminal

Figure 4.13 – WRIG fault current contribution for A-G fault with $R_f = 30\Omega$

As shown in the figure, the magnitude of the fault current flowing from the grid side terminal is close to 5kA, much higher than the current flowing from the wind farm

plant. Similar to the SCIG wind farm plant system, the fault current contributed by the wind farm plant is not very different from its pre-fault current. Therefore, voltage and current data captured at the grid side terminal makes one-end methods a better method to estimate the fault location than two-end methods.

Table 4.6 – WRIG wind farm fault location estimation for B-C fault

BC fault	+VE Reactance Method	Takagi Method	-VE Method	ABC Method
$R_f = 0\Omega$	49.99%	49.99%	38.88%	50.08%
$R_f = 5\Omega$	50.03%	49.99%	39.41%	44.49%
$R_f = 10\Omega$	50.06%	49.98%	38.71%	45.04%
$R_f = 30\Omega$	50.24%	49.92%	38.45%	55.85%
$R_f = 50\Omega$	50.42%	49.77%	37.15%	58.50%
$R_f = 100\Omega$	51.44%	49.66%	37.88%	59.13%

Table 4.6 shows the fault location estimation for B-C fault with different fault resistance. Figure 4.14 represents the fault location estimation error for WRIG-based wind power plant during a phase B to phase C fault.

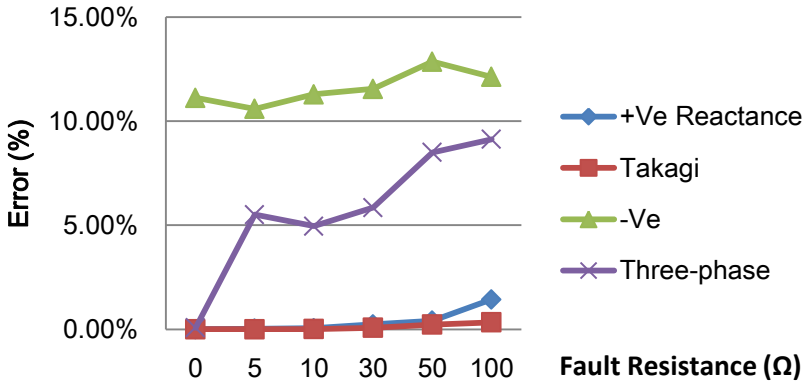

Figure 4.14 – WRIG wind farm fault location estimation error for B-C fault

Positive-sequence-reactance method and Takagi method still provides better fault location estimation than the other two methods with nearly 1% error. It is noted that

negative-sequence method gives the estimation with 12.22% error when the fault resistance is 100 Ω.

Figure 4.15 shows the fault current captured at both terminals of the line during a phase B-C fault with a 30 Ω fault resistance.

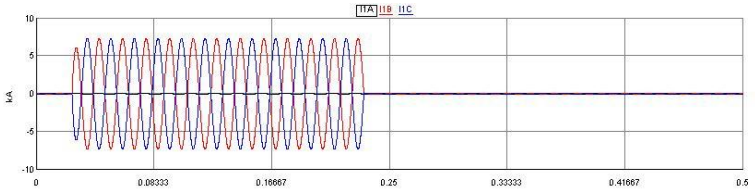

(a) Fault current contribution from the grid terminal

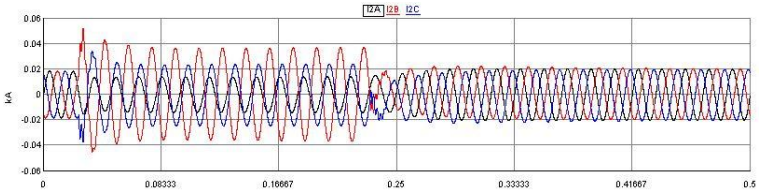

(b) Fault current contribution from the wind plant terminal

Figure 4.15 – WRIG fault current contribution for B-C fault with $R_f = 30\Omega$

The post-fault current contributed from the wind farm plant is three times the magnitude of the pre-fault current. Similar to A-G fault, the fault current contributed from the wind farm plant is much lower than the current from the grid but not very different from the pre-fault current.

Table 4.7 – WRIG wind farm fault location estimation for B-C-G fault

BCG fault	+VE Reactance Method	Takagi Method	-VE Method	ABC Method
$R_f = 0\Omega$	50.01%	50.01%	38.77%	48.00%
$R_f = 5\Omega$	50.06%	49.97%	39.27%	47.70%
$R_f = 10\Omega$	50.13%	49.93%	38.68%	52.47%
$R_f = 30\Omega$	50.58%	49.72%	38.75%	53.69%
$R_f = 50\Omega$	51.18%	49.40%	38.38%	53.84%
$R_f = 100\Omega$	54.21%	48.95%	37.96%	53.11%

Table 4.7 shows the fault location estimation for B-C-G fault with different fault resistance. Figure 4.16 represents the fault location estimation error for WRIG-based wind power plant during a phase B and C to ground fault.

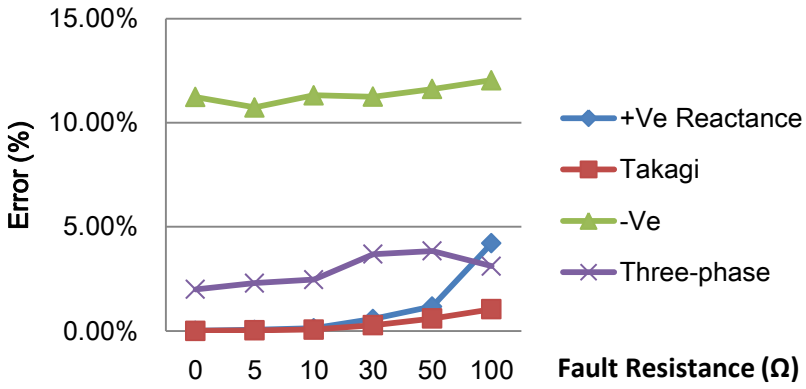

Figure 4.16 – WRIG wind farm fault location estimation error for B-C-G fault

Positive-sequence-reactance method provides fault location estimation of less than 5% error, while Takagi method can estimate fault location with nearly 1% error. Compared with one-end methods, two-end methods provide less accurate results. Negative-sequence method gives estimation with nearly 10% error and three-phase impedance method with nearly 5% error. Figure 4.17 shows the fault current captured at both terminals of the line during a phase B-C to ground fault with a 30 Ω fault resistance.

With a different fault resistance, the fault current contribution from both terminals follows the same pattern as mentioned during A-G fault.

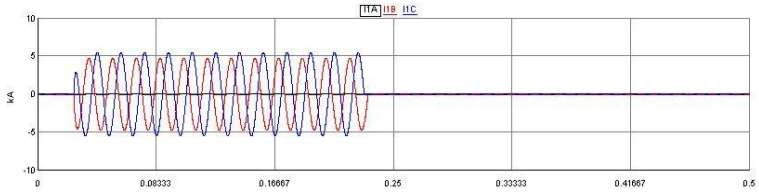

(a) Fault current contribution from the grid terminal

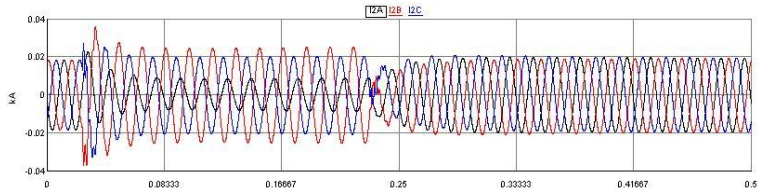

(b) Fault current contribution from the wind plant terminal

Figure 4.17 – WRIG fault current contribution for B-C-G fault with $R_f = 30\Omega$

The post-fault current contributed from the wind farm plant is less than twice the magnitude of the pre-fault current. Similarly, the fault current contributed from the wind farm plant is much lower than the current from the grid.

Table 4.8 – WRIG wind farm fault location estimation for three-phase fault

ABC fault	+VE Reactance Method	Takagi Method	-VE Method	ABC Method
$R_f = 0\Omega$	50.01%	50.01%	NA	50.01%
$R_f = 5\Omega$	50.01%	49.91%	NA	50.00%
$R_f = 10\Omega$	50.03%	49.82%	NA	50.00%
$R_f = 30\Omega$	50.27%	49.45%	NA	50.00%
$R_f = 50\Omega$	50.77%	49.06%	NA	50.00%
$R_f = 100\Omega$	53.22%	48.12%	NA	50.00%

Table 4.8 shows the fault location estimation for three-phase fault with different fault resistance. Figure 4.18 represents the fault location estimation error for WRIG-based wind power plant during a three-phase fault.

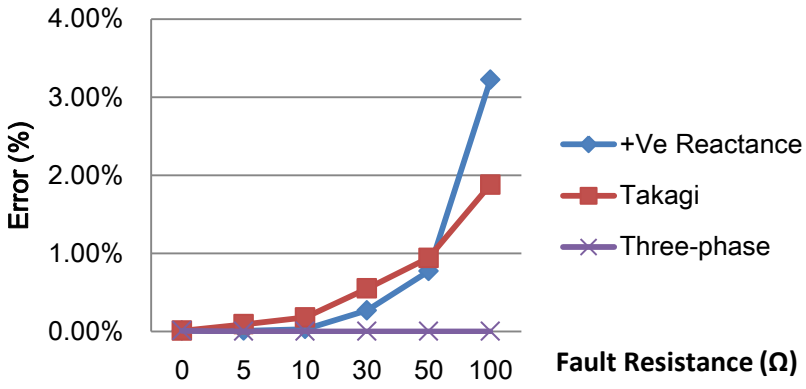

Figure 4.18 – WRIG wind farm fault location estimation error for three-phase fault

Negative-sequence method is not applied to this type of fault because negative-sequence component does not exist during a symmetrical fault. Similar to the SCIG wind farm simulation, three-phase impedance method provides a better estimation for symmetrical fault. Figure 4.19 shows the fault current captured at both terminals of the line during three-phase fault with a 30 Ω fault resistance.

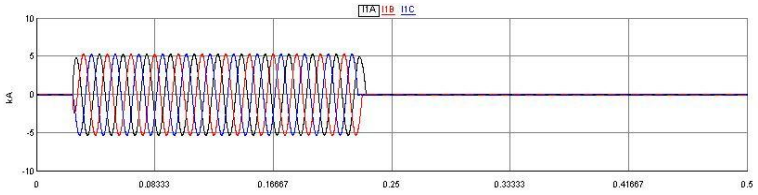

(a) Fault current contribution from the grid terminal

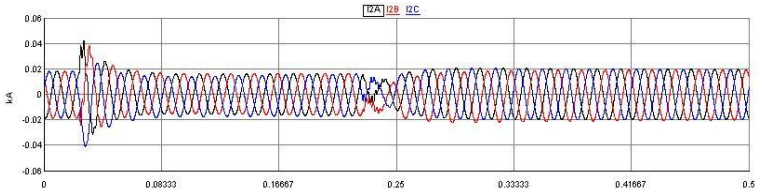

(b) Fault current contribution from the wind plant terminal

Figure 4.19 – WRIG fault current contribution for three-phase fault with $R_f = 30\Omega$

The wind farm plant equipped with SCIGs is very similar to the wind farm plant equipped with WRIGs. It can be observed that the fault location estimations performed by negative-sequence method in WRIG wind farm plant system are less accurate than in SCIG wind farm plant system. By negative-sequence method, the maximum error in SCIG wind farm plant system is 7.23% for B-C-G fault with 100 Ω fault resistance, while the maximum error in WRIG wind farm plant system is 12.85% for B-C fault with 50 Ω fault resistance. The reason is that the existence of external rotor resistance has an impact on the negative-sequence impedance of the wind farm plant. Therefore, the overall negative-sequence impedance at the receiving terminal depends on the speed of the wind turbine.

4.3 DFIG Wind Generator Simulation

The third equivalent system at terminal R is modeled as wind generator equipped with DFIG, as shown in Figure 4.20.

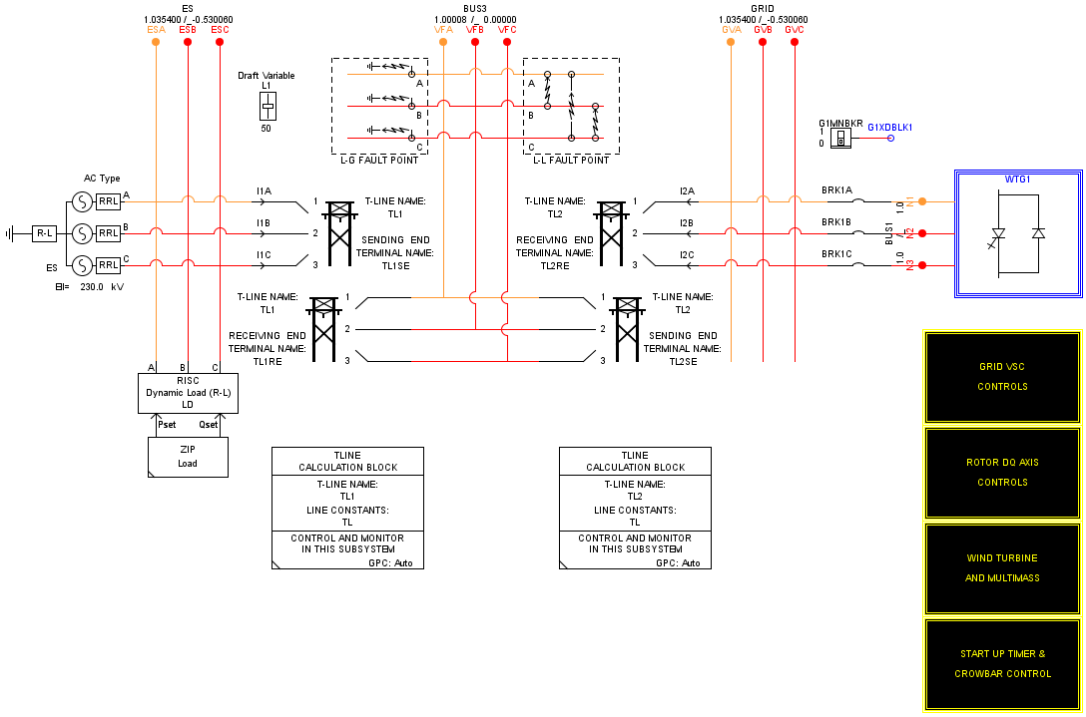

Figure 4.20 – DFIG wind generator simulation system in RSCAD

When a fault occurs on the transmission line and the rotor current of the induction generator exceeds the limit, the crowbar control will be activated to protect the back-to-back converter. If so, the *d*-*q* axis rotor current will not be controlled independently and the DFIG will operate similar to SCIG. Therefore, the derivation of negative-sequence impedance for SCIG is also acceptable to the DFIG under fault condition. With the DFIG parameters given in Table 3.2, the negative-sequence impedance of the DFIG is $Z_{neg} = 0.0075 + j0.1863$ in per unit value on the base of 2.2MVA and 0.69kV.

The same fault location occurrence and fault time duration are applied to this simulation system and the results are listed in Table 4.9 through Table 4.12.

Table 4.9 – DFIG wind farm fault location estimation for A-G fault

AG fault	+VE Reactance Method	Takagi Method	-VE Method	ABC Method
$R_f = 0\Omega$	49.84%	49.84%	71.36%	49.75%
$R_f = 5\Omega$	49.86%	49.91%	79.83%	51.07%
$R_f = 10\Omega$	49.85%	49.93%	82.37%	52.37%
$R_f = 30\Omega$	49.63%	49.85%	84.90%	54.03%
$R_f = 50\Omega$	49.34%	49.70%	85.41%	54.18%
$R_f = 100\Omega$	51.45%	52.19%	84.44%	54.44%

Table 4.9 shows the fault location estimation for A-G fault with different fault resistance. Figure 4.21 represents the fault location estimation error for WRIG-based wind power plant during a A-G fault.

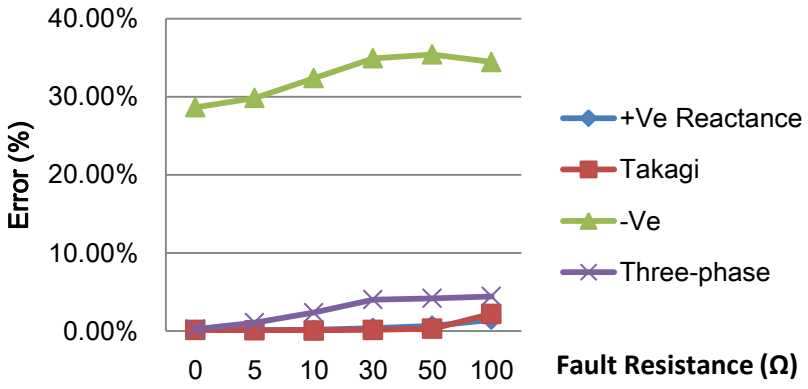

Figure 4.21 – DFIG wind farm fault location estimation error for A-G fault

The fault location estimation of positive-sequence-reactance method and Takagi method estimate the fault location with nearly 2% error, more accurate than the estimation of negative-sequence and three-phase method.

Figure 4.22 shows the fault current captured at both terminals of the line during a phase A to ground fault with a 30 Ω fault resistance. With a different fault resistance, the fault current contribution from the grid follows the same pattern but different magnitude

while the fault current contribution from the wind farm plant is found to be similar both in pattern and magnitude.

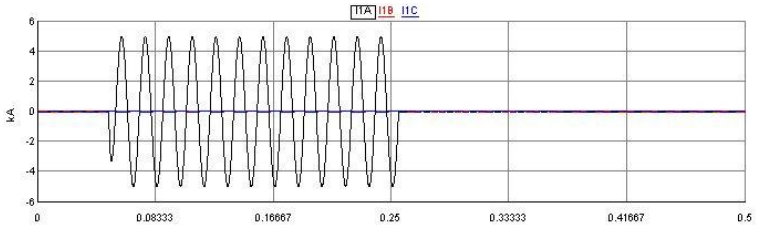

(a) Fault current contribution from the grid terminal

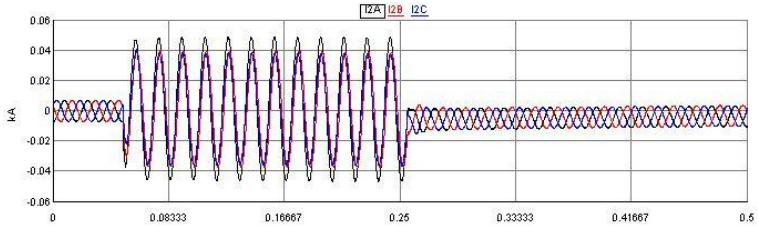

(b) Fault current contribution from the wind plant terminal

Figure 4.22 – DFIG fault current contribution for A-G fault with $R_f = 30\Omega$

As shown in the figure, the magnitude of the fault current flowing from the grid side terminal is close to 4.5kA, much higher than the current flowing from the wind farm plant. The fault current contributed by the wind farm plant is not very different from its pre-fault current.

It is observed that negative-sequence method provides estimation with more than 30% error. The reason for such a large error is because of the structure of the DFIG. The introduction of the back-to-back converter makes it even more difficult to determine the negative-sequence impedance for the use of negative-sequence method.

Table 4.10 – DFIG wind farm fault location estimation for B-C fault

BC fault	+VE Reactance Method	Takagi Method	-VE Method	ABC Method
$R_f = 0\Omega$	49.98%	49.98%	85.50%	49.94%
$R_f = 5\Omega$	49.46%	49.44%	84.25%	47.40%
$R_f = 10\Omega$	50.89%	50.86%	85.44%	44.44%
$R_f = 30\Omega$	50.31%	50.24%	85.90%	33.38%
$R_f = 50\Omega$	50.52%	50.42%	85.85%	29.90%
$R_f = 100\Omega$	50.93%	50.76%	85.17%	27.39%

Table 4.10 shows the fault location estimation for B-C fault with different fault resistance. Figure 4.23 represents the fault location estimation error for WRIG-based wind power plant during B-C fault.

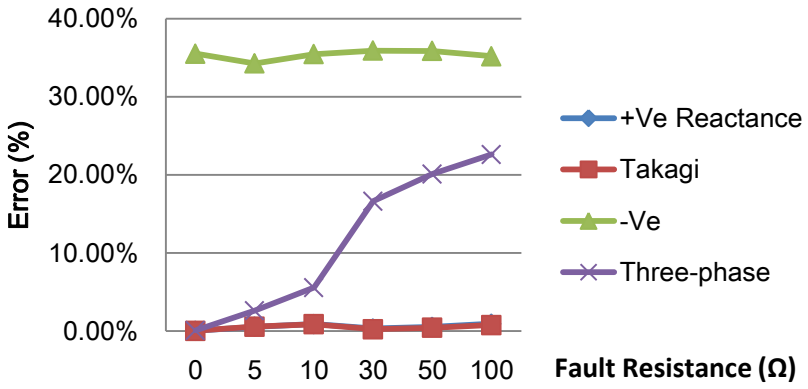

Figure 4.23 – DFIG wind farm fault location estimation error for B-C fault

Positive-sequence-reactance method and Takagi method provides fault location estimation with nearly 1% error. The error of fault location estimation of negative-sequence method is more than 40% when the fault resistance no matter the fault resistance. Similar to the other type of wind farm plant, three-phase impedance method does not provide more accurate estimation of the fault location.

Figure 4.24 shows the fault current captured at both terminals of the line during a A-G fault with a 30 Ω fault resistance.

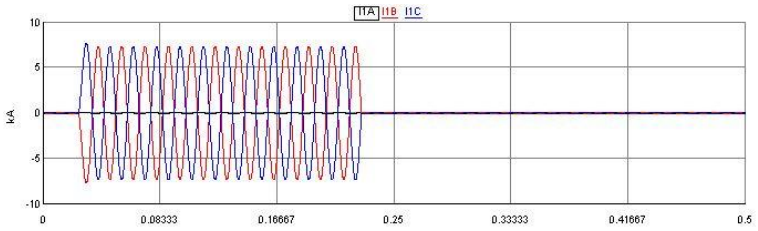

(a) Fault current contribution from the grid terminal

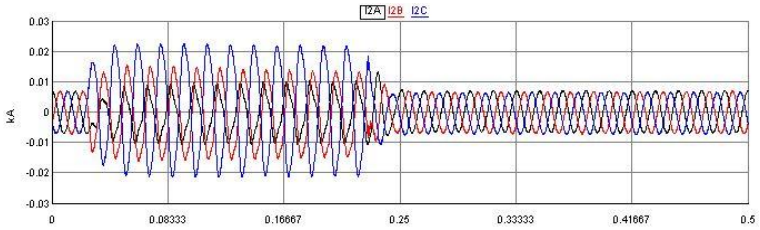

(b) Fault current contribution from the wind plant terminal

Figure 4.24 – DFIG fault current contribution for B-C fault with $R_f = 30\Omega$

The post-fault current contributed from the wind farm plant is twice the magnitude of the pre-fault current. Similar to A-G fault, the fault current contributed from the wind farm plant is much lower than the current from the grid.

Table 4.11 – DFIG wind farm fault location estimation for B-C-G fault

BCG fault	+VE Reactance Method	Takagi Method	-VE Method	ABC Method
$R_f = 0\Omega$	50.22%	50.22%	73.36%	49.85%
$R_f = 5\Omega$	49.96%	49.93%	71.20%	44.94%
$R_f = 10\Omega$	50.12%	50.06%	74.75%	41.75%
$R_f = 30\Omega$	50.45%	50.31%	84.88%	41.69%
$R_f = 50\Omega$	50.36%	50.17%	82.31%	42.33%
$R_f = 100\Omega$	51.41%	51.09%	87.48%	42.62%

Table 4.11 shows the fault location estimation for B-C-G fault with different fault resistance. Figure 4.25 represents the fault location estimation error for WRIG-based wind power plant during B-C-G fault.

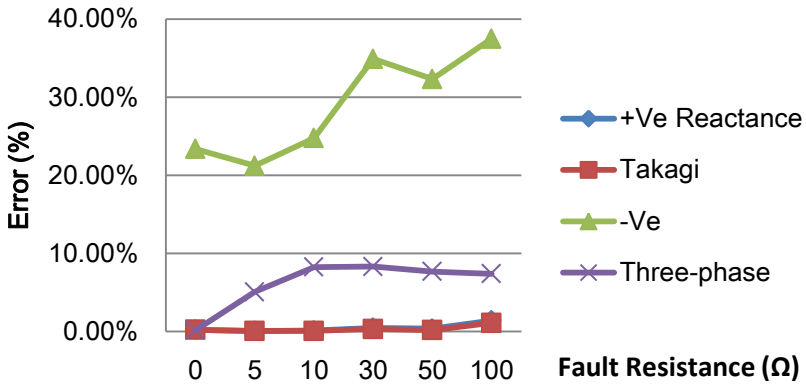

Figure 4.25 – DFIG wind farm fault location estimation error for B-C-G fault

Positive-sequence-reactance method and Takagi method provide fault location estimation of nearly 2% error. Similar to the previous fault types, positive-sequence-reactance method and Takagi method provides better fault location estimation than negative-sequence method and three-phase impedance method. Figure 4.26 shows the fault current captured at both terminals of the line during a B-C-G fault with a 30 Ω fault resistance.

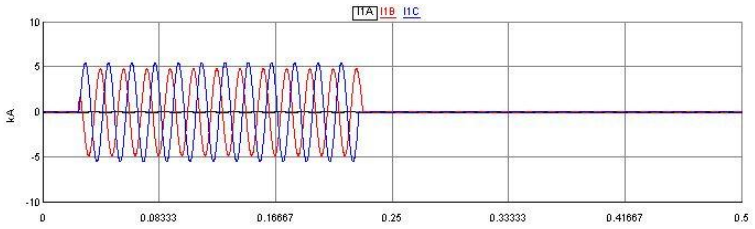

(a) Fault current contribution from the grid terminal

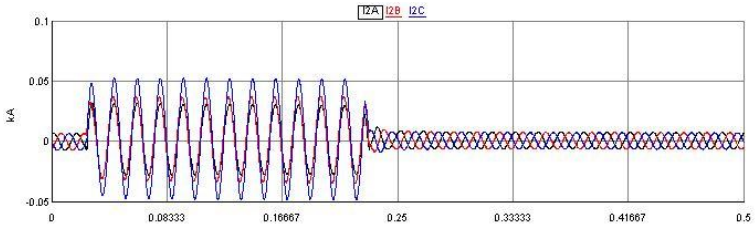

(b) Fault current contribution from the wind plant terminal

Figure 4.26 – DFIG fault current contribution for B-C-G fault with $R_f = 30\Omega$

The post-fault current contributed from the wind farm plant is nearly 6 times the magnitude of the pre-fault current. Similarly, the fault current contributed from the wind farm plant is much lower than the current from the grid.

Table 4.12 – DFIG wind farm fault location estimation for three-phase fault

ABC fault	+VE Reactance Method	Takagi Method	-VE Method	ABC Method
$R_f = 0\Omega$	50.07%	50.07%	NA	50.02%
$R_f = 5\Omega$	50.05%	49.95%	NA	50.01%
$R_f = 10\Omega$	50.10%	49.89%	NA	50.02%
$R_f = 30\Omega$	50.38%	49.55%	NA	50.02%
$R_f = 50\Omega$	50.99%	49.27%	NA	50.01%
$R_f = 100\Omega$	53.63%	48.51%	NA	50.02%

Table 4.12 shows the fault location estimation for three-phase fault with different fault resistance. Figure 4.27 represents the fault location estimation error for WRIG-based wind power plant during a three-phase fault.

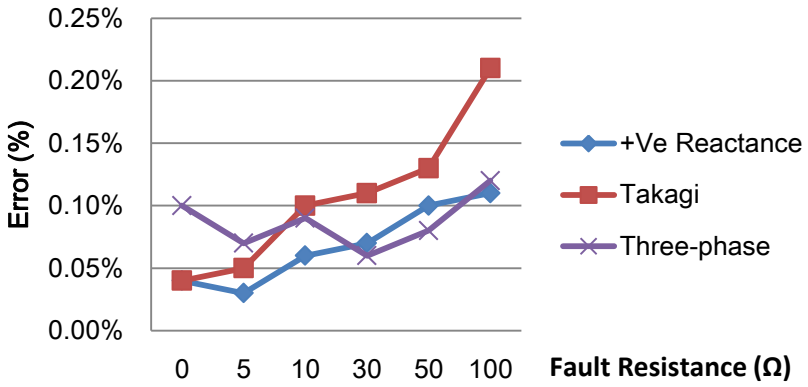

Figure 4.27 – DFIG wind farm fault location estimation error for three-phase fault

Negative-sequence method is not applied to this type of fault because negative-sequence component does not exist during a symmetrical fault. Figure 4.28 shows the fault current at both terminals of the line during a three-phase fault with a 30 Ω fault resistance.

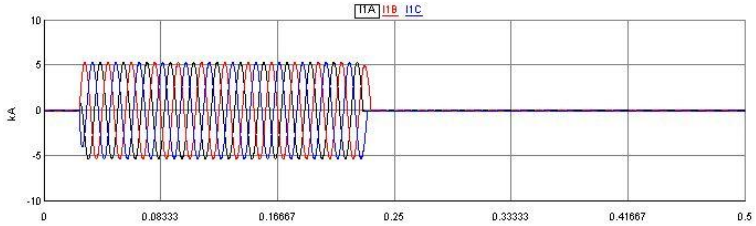

(a) Fault current contribution from the grid terminal

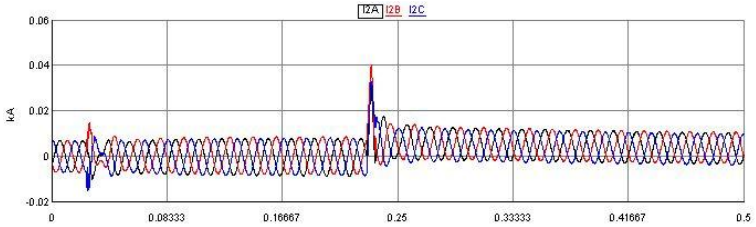

(b) Fault current contribution from the wind plant terminal

Figure 4.28 – DFIG fault current contribution for three-phase fault with $R_f = 30\Omega$

If we compare these results with the fault location estimation performed in Chapter 2, we can find an interesting comparison between a conventional power grid and a power grid with wind farm plant connection. Negative-sequence method and three-phase impedance method provide better fault location estimation than positive-sequence-reactance method and Takagi method for a transmission line in a conventional power grid. On the contrary, positive-sequence-reactance method and Takagi method provide better estimation than negative-sequence method and three-phase impedance method for a power grid with wind power penetration.

For one-end methods, both positive-sequence-reactance method and Takagi method can provide good fault location estimation for a transmission line connecting wind farm as long as the fault current contribution from the grid side is much higher than from the wind farm side. This is usually true if a wind farm is connected to a robust and strong power system. Takagi method can provide even better estimation than positive-sequence-reactance method for the consideration of pre-fault current.

For two-end methods, negative-sequence method provides fault location estimation with acceptable error for wind farm equipped with SCIGs, but much larger error for wind farm with WRIGs and DFIGs. The absence of an accurate calculation of the equivalent negative-sequence impedance is the main reason that negative-sequence method is not able to locate the fault for a transmission line with wind farm connection. Three-phase impedance method can estimate fault location with high accuracy if the fault is symmetrical, but not as accurate as one-end method if unsymmetrical faults occur. The

use of least-square estimation is the major source of error, especially when the fault resistance is high.

CHAPTER FIVE

CONCLUSION AND FUTURE RESEARCH

Modern power systems are expanding and growing to a large interconnected system. The occurrence of faults and disturbances are inevitable in this complex network. Utilities are required to provide continuous and reliable power supply to customers. If a power outage happens, it is expected to recover the power as soon as possible. An effective fault location estimation technique can greatly improve the operation of a power system and provide useful information for fault analysis. Different fault location estimation methods have been merged into modern digital protective relays for distance protection. Among the techniques that have been developed and applied, impedance-based fault location methods are considered as effective and economical. They have done a good job in identifying fault types and fault location for transmission lines in conventional power systems. However, the penetration of wind farm plants has brought many challenges to conventional power systems. Therefore, the effectiveness of the existing impedance-based fault location methods for a transmission line connecting a commercial wind farm should be examined and verified.

This thesis provides the validation of existing impedance-based fault location methods for transmission line connected with wind farm plants. Detailed wind farm models were developed and simulated on a real-time digital simulator. These models can also be used for research on wind generation. In addition, the application of PMUs and synchronized phasor measurements improves the accuracy of the fault location estimation.

In Chapter 2, the principles of four impedance-based fault location methods were reviewed. Positive-sequence-reactance method and the Takagi method were defined as one-end method. Negative-sequence method and three-phase method were defined as two-end method. One-end methods use only voltage and current information captured at one terminal of the line to estimate the fault location, while two-end methods require information from both terminals. The four methods were applied to a transmission line connecting two equivalent sources to verify the accuracy of fault location estimation in conventional power systems. This was performed on RTDS with real-time simulation. Results showed that the estimations by positive-sequence-reactance method and Takagi method were significantly affected by fault resistance, while negative-sequence method and three-phase impedance method gave accurate estimation regardless of fault resistance. Therefore, it was concluded that two-end methods can provide much more accurate fault location estimation than one-end methods for a transmission line connecting conventional sources. In order to validate the effectiveness of these impedance-based methods in a system with wind farm penetration, three types of wind farm plant models were explained in detail in Chapter 3.

Commercial wind power plants equipped with three different types of wind turbine generators were applied to demonstrate the impact of wind penetration. SCIG was a fixed-speed type and required pitch angle control to maintain the turbine speed at a constant value. WRIG was a variable-speed type wind turbine generator that allowed a variable slip in a certain range up to 5%. This change made WRIG a more active type of generator than SCIG in speed control. With the help of a back-to-back converter, DFIG

was able to have a variable slip in a wide range up to 30% so that the active and reactive power output can be independently controlled through vector control scheme. Crowbar control and pitch angle control were also included to protect the converter and manage optimal power output.

Each wind farm model illustrated in Chapter 3 was connected to the conventional power grid through a transmission line to validate the fault location methods mentioned in Chapter 2. The results for different types of fault and various fault resistance were listed and discussed in Chapter 4.

For a transmission line connecting the power grid with a wind farm plant, both the positive-sequence-reactance method and the Takagi method provided accurate fault location estimation with less than 2% error. The Takagi method has less error in estimating fault location if the pre-fault current is considered. The accuracy of negative-sequence method estimation significantly relied on the accuracy of equivalent negative-sequence impedance of the wind plant. Among the three types of wind farm plants, negative-sequence method estimation for SCIG-based wind plants had a higher accuracy than WRIG-based and DFIG-based wind plants. The addition of external rotor resistance and back-to-back power electronics converter introduced uncertainty of the negative-sequence impedance. Therefore, it is not practical to apply negative-sequence method to transmission lines connected with wind farm plants. The three-phase impedance method provided good estimation for symmetrical faults but not for unsymmetrical faults. This method was based on least-square estimation. The fault current contribution from the wind farm plant was not very different from its pre-fault

current regardless of the fault resistance. Thus, this method is less accurate than the positive-sequence-reactance and the Takagi method.

Based on the presented results, it can be concluded that accurate fault location estimation may be determined by voltage and current data captured only at the grid side as long as the wind farm plant is connected to a robust and strong power system. This strong power system contributes a much higher fault current than the wind farm plant during a fault condition.

In this thesis, a wind farm plant equipped with SCIGs and WRIGs was modeled by only three separate wind turbines, while a DFIG-based wind plant was modeled by one wind turbine. For future research, it is expected that more numbers of wind turbines can be added to represent a real commercial wind farm plant. In addition, the power grid was simulated by a simplified equivalent source. A detailed power grid model can be implemented in RSCAD to represent a more practical renewable energy network if real system data is available.

APPENDICES

Appendix A

Flow Chart of the Fault Location Estimation Algorithms

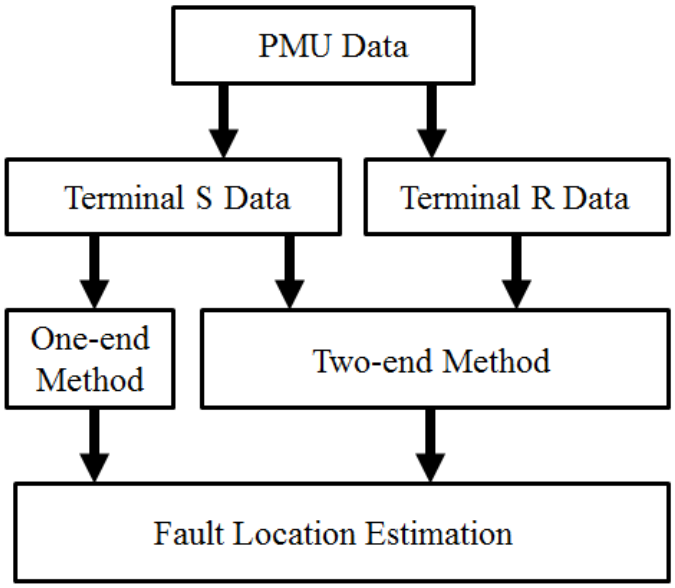

Appendix B

Fault Location Algorithm in MATLAB

```
clear all
clc

i=sqrt(-1); % imaginary part
t=exp(i*120*pi/180); % transformation vector
T=[1 1 1;1 t^2 t;1 t t^2]; % transformation matrix of sequence component

% system data
ZL1=50*(0.025+i*0.15); % positive-sequence impedance of the line
ZL2=50*(0.025+i*0.15); % negative-sequence impedance of the line
ZL0=50*(0.075+i*0.45); % zero-sequence impedance of the line
ZLabc=T*diag([ZL0 ZL1 ZL2])*T^-1; % phase component of the line impedance
ZS2=10*exp(i*80*pi/180); % negative-sequence impedance of the wind plant

Rs=0.0077; % stator resistance of the induction generator in per unit
Xs=i*0.0697; % stator reactance of the induction generator in per unit
Xm=i*3.454; % magnetizing reactance of the induction generator in per unit
Rr=0.0062; % rotor resistance of the induction generator in per unit
Xr=i*0.0834; % rotor reactance of the induction generator in per unit
X_PMT=i*0.08*10/2; % reactance of the pad-mounted transformer in per unit
X_SUB=i*0.08; % reactance of the substation transformer in per unit
ZWT2=(10/1.808)*(Rs+Xs+Xm*(Rr/2+Xr)/(Xm+Rr/2+Xr)); % equivalent
negative-sequence impedance of the induction generator in per unit
ZR2=((1/3)*(ZWT2+X_PMT)+X_SUB)*(230^2/10); % total equivalent
negative-sequence impedance of the wind plant
k=ZL0/ZL1-1; % correction factor

% PMU data reading into the program
[TIME,ISA_ANG,ISA_MAG,ISB_ANG,ISB_MAG,ISC_ANG,ISC_MAG,VSA_ANG,VSA_MAG,V
SB_ANG,VSB_MAG,VSC_ANG,VSC_MAG,IRA_ANG,IRA_MAG,IRB_ANG,IRB_MAG,IRC_ANG,
IRC_MAG,VRA_ANG,VRA_MAG,VRB_ANG,VRB_MAG,VRC_ANG,VRC_MAG]=textread('T1-A
G-R0-ABC.out','%f %f %f %f %f %f %f %f %f %f %f %f %f %f %f %f %f %f %f
 %f %f %f %f %f %f');
[TIME,IS0_ANG,IS0_MAG,IS1_ANG,IS1_MAG,IS2_ANG,IS2_MAG,VS0_ANG,VS0_MAG,V
S1_ANG,VS1_MAG,VS2_ANG,VS2_MAG,IR0_ANG,IR0_MAG,IR1_ANG,IR1_MAG,IR2_ANG,
IR2_MAG,VR0_ANG,VR0_MAG,VR1_ANG,VR1_MAG,VR2_ANG,VR2_MAG]=textread('T1-A
G-R0-012.out','%f %f %f %f %f %f %f %f %f %f %f %f %f %f %f %f %f %f %f
 %f %f %f %f %f %f');

% +VE reactance algorithm
D1=zeros(156,1); % 156 samples
% 156 iterations for fault location estimation
for m=1:1:156
    Vsa=VSA_MAG(m)*10^3*exp(i*VSA_ANG(m));
    Isa=ISA_MAG(m)*10^3*exp(i*ISA_ANG(m));
    Is0=(1/3)*IS0_MAG(m)*10^3*exp(i*IS0_ANG(m));
    Is=Isa+k*Is0;
    D1(m)=imag(Vsa/Is)/imag(ZL1);
```

```
end
D1;
D1(40)

% Takagi algorithm
D2=zeros(156,1); % 156 samples
% 156 iterations for fault location estimation
for m=1:1:156
    Vsa=VSA_MAG(m)*10^3*exp(i*VSA_ANG(m));
    Isa=ISA_MAG(m)*10^3*exp(i*ISA_ANG(m));
    Isa_pre=ISA_MAG(1)*10^3*exp(i*ISA_ANG(1));
    Isup=Isa-Isa_pre;
    Is0=(1/3)*IS0_MAG(m)*10^3*exp(i*IS0_ANG(m));
    Is=Isa+k*Is0;
    D2(m)=imag(Vsa*conj(Isup))/imag(ZL1*Is*conj(Isup));
end
D2;
D2(40)

% Negative-sequence algorithm
D3=zeros(156,1); % 156 samples
syms x
% 156 iterations for fault location estimation
for m=1:1:156
    Is2=IS2_MAG(m)*10^3*exp(i*IS2_ANG(m));
    Ir2=IR2_MAG(m)*10^3*exp(i*IR2_ANG(m));
    a=real(Is2*ZS2);
    b=imag(Is2*ZS2);
    c=real(Is2*ZL2);
    d=imag(Is2*ZL2);
    e=real(ZL2+ZR2);
    f=imag(ZL2+ZR2);
    g=real(ZL2);
    h=imag(ZL2);
    A=abs(Ir2)^2*(g^2+h^2)-(c^2+d^2);
    B=-2*abs(Ir2)^2*(e*g+f*h)-2*(a*c+b*d);
    C=abs(Ir2)^2*(e^2+f^2)-(a^2+b^2);
    temp=eval(solve(A*x^2+B*x+C));
    for n=1:1:2
        if(temp(n)>=0&&temp(n)<=1)
            D3(m)=temp(n);
        else
        end
    end
end
D3;
D3(40)

% Direct Zabc algorithm
D4=zeros(156,1); % 156 samples
% 156 iterations for fault location estimation
for m=1:1:156
    Vsa=VSA_MAG(m)*10^3*exp(i*VSA_ANG(m));
```

```
    Vsb=VSB_MAG(m)*10^3*exp(i*VSB_ANG(m));
    Vsc=VSC_MAG(m)*10^3*exp(i*VSC_ANG(m));
    Isa=ISA_MAG(m)*10^3*exp(i*ISA_ANG(m));
    Isb=ISB_MAG(m)*10^3*exp(i*ISB_ANG(m));
    Isc=ISC_MAG(m)*10^3*exp(i*ISC_ANG(m));
    Vs=[Vsa;Vsb;Vsc];
    Is=[Isa;Isb;Isc];
    Vra=VRA_MAG(m)*10^3*exp(i*VRA_ANG(m));
    Vrb=VRB_MAG(m)*10^3*exp(i*VRB_ANG(m));
    Vrc=VRC_MAG(m)*10^3*exp(i*VRC_ANG(m));
    Ira=IRA_MAG(m)*10^3*exp(i*IRA_ANG(m));
    Irb=IRB_MAG(m)*10^3*exp(i*IRB_ANG(m));
    Irc=IRC_MAG(m)*10^3*exp(i*IRC_ANG(m));
    Vr=[Vra;Vrb;Vrc];
    Ir=[Ira;Irb;Irc];
    left=Vs-Vr+ZLabc*Ir;
    right=ZLabc*(Is+Ir);

Y=[real(left(1));real(left(2));real(left(3));imag(left(1));imag(left(2)
);imag(left(3))];

M=[real(right(1));real(right(2));real(right(3));imag(right(1));imag(rig
ht(2));imag(right(3))];
    D4(m)=(M'*M)^-1*M'*Y;
end
D4;
D4(40)
```

REFERENCES

[1] M.M. Saha, J. Izykowski, and E. Rosolowski. *Fault Location on Power Networks.* 2010.

[2] *IEEE Guide for Determining Fault Location on AC Transmission and Distribution Lines.* IEEE Std C37.114-2004, 2005: p. 0_1-36.

[3] K. Zimmerman and D. Costello. *Impedance-Based Fault Location Experience*. in *Rural Electric Power Conference, 2006 IEEE*. 2006.

[4] T. Takagi, Y.Yamakoshi, M. Yamaura, R. Kondow, and T. Matsushima. *Development of a New Type Fault Locator Using the One-Terminal Voltage and Current Data.* Power Apparatus and Systems, IEEE Transactions on, 1982. **PAS-101**(8): p. 2892-2898.

[5] J. Izykowski, E. Rosolowski, and M.M. Saha. *Locating faults in parallel transmission lines under availability of complete measurements at one end.* Generation, Transmission and Distribution, IEE Proceedings-, 2004. **151**(2): p. 268-273.

[6] A.A. Girgis, C.M. Fallon, and D.L. Lubkeman, *A fault location technique for rural distribution feeders.* Industry Applications, IEEE Transactions on, 1993. **29**(6): p. 1170-1175.

[7] Y. G, and A. Guzman. *Distribution feeder fault location using IED and FCI information*. in *Protective Relay Engineers, 2011 64th Annual Conference for*. 2011.

[8] M. Choi, S. Lee, D. Lee, and B. Jin. *A new fault location algorithm using direct circuit analysis for distribution systems.* Power Delivery, IEEE Transactions on, 2004. **19**(1): p. 35-41.

[9] P.M. Anderson. *Analysis of Faulted Power Systems.* ISBN 0-7803-1145-0, The Institute of Electrical and Electronics Engineers, 1973.

[10] D.A. Tziouvaras, J.B. Roberts, and G. Benmouyal. *New multi-ended fault location design for two- or three-terminal lines*. in *Developments in Power System Protection, 2001, Seventh International Conference on (IEE)*. 2001.

[11] A.A. Girgis, D.G. Hart, and W.L. Peterson. *A new fault location technique for two- and three-terminal lines.* Power Delivery, IEEE Transactions on, 1992. **7**(1): p. 98-107.

[12] P.F. Gale, P. A. Crossley, and X. Bingyin. *Fault location based on travelling waves*. in *Developments in Power System Protection, 1993., Fifth International Conference on*. 1993.

[13] F.H. Magnago, and A. Abur. *Fault location using wavelets.* Power Delivery, IEEE Transactions on, 1998. **13**(4): p. 1475-1480.

[14] A.O. Ibe, and B.J. Cory. *A Traveling Wave-Based Fault Locator for Two-and Three-Terminal Networks.* Power Engineering Review, IEEE, 1986. **PER-6**(4): p. 55-55.

[15] Z.Q. Bo, G. Weller, and M.A. Redfern, *Accurate fault location technique for distribution system using fault-generated high-frequency transient voltage signals.* Generation, Transmission and Distribution, IEE Proceedings-, 1999. **146**(1): p. 73-79.

[16] K.K. Li, L.L. Lai, and A.K. David. *Application of artificial neural network in fault location technique*. in *Electric Utility Deregulation and Restructuring and Power Technologies, 2000. Proceedings. DRPT 2000. International Conference on*. 2000.

[17] Z. Galijasevic, and A. Abur, *Fault location using voltage measurements.* Power Delivery, IEEE Transactions on, 2002. **17**(2): p. 441-445.

[18] J.D. Ree, V. Centeno, and J.S. Thorp. *Synchronized Phasor Measurement Applications in Power Systems.* Smart Grid, IEEE Transactions on, 2010. **1**(1): p. 20-27.

[19] C. Fan, X. Du, S. Li, and W. Yu. *An Adaptive Fault Location Technique Based on PMU for Transmission Line*. in *Power Engineering Society General Meeting, 2007. IEEE*. 2007.

[20] V. Terzija, and M. Kezunovic. *Synchronised Measurement Technology for Analysis of Transmission Lines Faults*. in *System Sciences (HICSS), 2011 44th Hawaii International Conference on*. 2011.

[21] M. Korkali, and A. Abur. *Fault location in meshed power networks using synchronized measurements*. in *North American Power Symposium (NAPS), 2010*. 2010.

[22] A.H. Al-Mohammed, M.M. Mansour, and M.A. Abido. *Application of Phasor Measurement Units (PMUs) for fault location in SEC-EOA interconnected*

network. in *Energy Conference and Exhibition (EnergyCon), 2010 IEEE International*. 2010.

[23] *Global Wind Report - Annual Market Update 2010.* 2010.

[24] R. Piwko, P. Meibom, H. Holttinen, B. Shi, N. Miller, Y. Chi, and W. Wang. *Penetrating Insights: Lessons Learned from Large-Scale Wind Power Integration.* Power and Energy Magazine, IEEE, 2012. **10**(2): p. 44-52.

[25] R. Zavadil, N. Miller, A. Ellis, and E. Muljadi. *Making connections [wind generation facilities]*. Power and Energy Magazine, IEEE, 2005. **3**(6): p. 26-37.

[26] B. Fox, D. Flynn, L. Bryans, N. Jenkins , D. Milborrow, M. Malley, R.Watson, and O. Anays-Lara. *Wind Power Integration - Connection and System Operational Aspects.* 2007.

[27] R. Pena, J.C. Clare, and G.M. Asher, *Doubly fed induction generator using back-to-back PWM converters and its application to variable-speed wind-energy generation.* Electric Power Applications, IEE Proceedings -, 1996. **143**(3): p. 231-241.

[28] B.H. Chowdhury and S. Chellapilla. *Double-fed Induction Generator Control for Variable Speed Wind Power Generation.* Electric Power Systems Research, 2005.

[29] S.K. Salman and B. Badrzadeh. *New Approach for Modelling Doubly-Fed Induction Generator (DFIG) for Grid-connection Studies.*

[30] N. Samaan, R. Zavadil, J. C. Smith, and J. Conto. *Modeling of wind power plants for short circuit analysis in the transmission network*. in *Transmission and Distribution Conference and Exposition, 2008. T&D. IEEE/PES*. 2008.

[31] J. Morren, and S.W.H. de Haan, *Short-Circuit Current of Wind Turbines With Doubly Fed Induction Generator.* Energy Conversion, IEEE Transactions on, 2007. **22**(1): p. 174-180.

[32] R.Reginato, M.G. Zanchettin, and M. Tragueta. *Analysis of safe integration criteria for wind power with induction generators based wind turbines*. in *Power & Energy Society General Meeting, 2009. PES '09. IEEE*. 2009.

[33] RTDS Technologies, *Real-time Digital Simulator Manuals & Brochures, 2003.*

[34] V. Akhmatov. *Analysis of Dynamic Behaviour of Electric Power Systems with Large Amount of Wind Power.* PhD Dissertation, 2003.

[35] G. Byeon, I.K. Park, and G. Jang, *Modelling and Control of a Doubly-Fed Induction Generator (DFIG) Wind Power Generation System for Real-time Simulators.* Journal of Electrical Engineering & Technology, 2010. **5**(No. 1): p. 61~69.

[36] Q. Wei, G.K. Venayagamoorthy, and R.G. Harley, *Real-Time Implementation of a STATCOM on a Wind Farm Equipped With Doubly Fed Induction Generators.* Industry Applications, IEEE Transactions on, 2009. **45**(1): p. 98-107.

[37] P. C. Krause, O. Wasynczuk, and S. D. Sudhoff, *Analysis of Electric Machinery and Drive Systems.* 2002.

[38] C.-M. Ong. *Dynamic Simulation of Electric Machinery - Using Matlab/Simulink.* 1998.